

1                   **Rheologic constraints on the upper mantle from five years of**  
2                   **postseismic deformation following the El Mayor-Cucapah**  
3                   **earthquake**

4                   **T. T. Hines<sup>1</sup>, E. A. Hetland<sup>1</sup>**

5                   <sup>1</sup>Department of Earth and Environmental Sciences, University of Michigan, Ann Arbor, Michigan, USA.

6                   **Key Points:**

- 7                   • Transient postseismic deformation can be observed following the El Mayor-Cucapah  
8                   earthquake at epicentral distances of up to 400 km  
9                   • Near-field postseismic deformation exhibits early transience that decays to a sustained  
10                  rate which is elevated above the preseismic trend  
11                  • A Zener or Burgers upper mantle can explain far-field deformation while near-field tran-  
12                  sience can be described with afterslip

13 **Abstract**

14 Five years of postseismic deformation following the Mw=7.2 El Mayor-Cucapah earth-  
 15 quake reveals transient deformation that decays back to its pre-earthquake trend after about  
 16 three years at epicentral distances greater than  $\sim 200$  km. At shorter distances, the rapid trans-  
 17 sience decays to a sustained rate which exceeds its pre-earthquake trend. We attempt to de-  
 18 termine the mechanisms driving this deformation, where we consider afterslip at seismogenic  
 19 depths and viscoelastic relaxation in the lower crust and upper mantle as candidate mechanisms.  
 20 We find that early, rapid, near-field deformation can be explained with afterslip on the fault  
 21 that ruptured coseismically, while the later, sustained, near-field deformation can be explained  
 22 with either continued afterslip in an effectively elastic lower crust, or lower crustal viscoelas-  
 23 tic relaxation with a steady-state viscosity of  $\sim 10^{19}$  Pa s. The trend in far-field deformation  
 24 is best explained with a transient viscosity of  $\sim 10^{18}$  Pa s in the upper mantle. We argue that  
 25 a transient rheology in the mantle is preferable over a Maxwell rheology because it better pre-  
 26 dicts the decay in postseismic deformation, and also because it does not conflict with the gen-  
 27 erally higher, steady-state viscosities inferred from studies of geophysical processes occurring  
 28 over longer time-scales.

29 **1 Introduction**

30 Ground deformation in the years following a large ( $Mw \gtrsim 7$ ) earthquake can be used to  
 31 gain insight into the mechanical behavior of the crust and upper mantle. The interpretations  
 32 of postseismic deformation are not always conclusive because multiple postseismic deforma-  
 33 tion mechanisms, such as afterslip or viscoelastic relaxation in the lower crust and upper man-  
 34 tle, can have qualitatively similar surface expressions [e.g. Savage, 1990]. This complication  
 35 can potentially be remedied by having a sufficient number of well positioned observations of  
 36 the postseismic displacement field [Hearn, 2003]. Owing to the dense geodetic network de-  
 37 ployed throughout the 2000s as part of the Plate Boundary Observatory, the postseismic de-  
 38 formation following the April 4, 2010, Mw=7.2 El Mayor-Cucapah earthquake in Baja Cal-  
 39 ifornia was observed at more GPS stations than any other earthquake in California to date. With  
 40 such a large collection of data, we attempt to discern the mechanisms driving postseismic de-  
 41 formation following the El Mayor-Cucapah earthquake.

42 Here is some background on the El Mayor Earthquake

43 Previous studies which have modeled postseismic deformation following the El Mayor-  
 44 Cucapah earthquake include Pollitz *et al.* [2012], Gonzalez-Ortega *et al.* [2014], Spinler *et al.*  
 45 [2015], and Rollins *et al.* [2015]. Of these studies, Gonzalez-Ortega *et al.* [2014] and Rollins  
 46 *et al.* [2015] have attempted to describe the postseismic deformation with afterslip in an elas-  
 47 tic half-space. Gonzalez-Ortega *et al.* [2014] described five months of postseismic deforma-  
 48 tion, observed by InSAR and GPS within  $\sim 50$  km of the rupture, with afterslip and contrac-  
 49 tion on the coseismically ruptured fault. Gonzalez-Ortega *et al.* [2014] noted that their preferred  
 50 model underestimated the GPS displacements for stations  $\gtrsim 25$  km from the rupture and sug-  
 51 gested that it could be the result of unmodeled viscoelastic relaxation. Using only continuous  
 52 GPS stations, which are mostly north of the rupture zone, Rollins *et al.* [2015] found that three  
 53 years of postseismic deformation can be adequately explained by afterslip, albeit with an im-  
 54 plausibly large amount of slip inferred on the least constrained, southern-most fault segment.  
 55 Here, we suggest the afterslip inferred by Rollins *et al.* [2015] may have been acting as a proxy  
 56 for distributed relaxation in the upper mantle.

57 Pollitz *et al.* [2012], Rollins *et al.* [2015] and Spinler *et al.* [2015] have explored viscoelas-  
 58 tic relaxation in the lower crust and upper mantle as a potential postseismic deformation mech-  
 59 anism. The rheology of the crust and mantle is largely unknown and so modeling postseis-  
 60 mic deformation with viscoelastic relaxation requires one to assume a rheologic model and  
 61 then find the best fitting rheologic parameters. The inference of these rheologic parameters is  
 62 a computationally expensive non-linear inverse problem which is typically approached with

a forward modeling grid search method. Consequently, a simplified structure for the Earth must be assumed in order to minimize the number of rheologic parameters that need to be estimated. For example, it is commonly assumed that the lower crust and upper mantle are homogeneous, Maxwell viscoelastic layers, which may be too simplistic for postseismic studies [Riva and Govers, 2009; Hines and Hetland, 2013]. To further reduce the dimensions of the model space, it is also necessary to make simplifying assumptions about the behavior of afterslip. For example, one can assume a frictional model for afterslip and parametrize afterslip in terms of the unknown rheologic properties of the fault [e.g. Johnson *et al.*, 2009; Johnson and Segall, 2004]. One can also assume that afterslip does not persist for more than a few months and then model the later postseismic deformation assuming it to be the result of only viscoelastic relaxation [e.g. Pollitz *et al.*, 2012; Spinler *et al.*, 2015]. However, postseismic afterslip in similar tectonic settings has been observed to persist for decades following earthquakes [Çakir *et al.*, 2012; Cetin *et al.*, 2014]. Indeed, the preferred viscoelastic model from Pollitz *et al.* [2012] significantly underestimates deformation in the Imperial Valley, which could be indicative of unmodeled continued afterslip. Neglecting to allow for sustained afterslip as a postseismic mechanism could then lead to biased inferences of viscosities.

In this study, we perform a kinematic inversion for fault slip, allowing it to persist throughout the postseismic period, while simultaneously estimating the viscosity of the lower crust and upper mantle. We create an initial model of the fault slip and effective viscosity necessary to describe early postseismic deformation using the method described in Hines and Hetland [2016]. This method utilizes a first-order approximation of surface deformation resulting from viscoelastic relaxation which is only applicable to the early postseismic period. In this case, our initial model describes the first 0.8 years of postseismic deformation following the El Mayor-Cucapah earthquake. We then use the inferred effective viscosity structure from the initial model to create a suite of postseismic models to explain the five years of postseismic data available to date. Of the suite of models tested, we find that postseismic deformation following the El Mayor-Cucapah earthquake can be explained with a combination of afterslip on a fault segment running through the Sierra Cucapah and a Zener rheology in the upper mantle with a transient viscosity that decays from  $6 \times 10^{18}$  Pa s to  $1 \times 10^{18}$  Pa s at 120 km depth.

## 2 Data Processing

We use continuous GPS position time series provided by University Navstar Consortium (UNAVCO) for stations within a 400 km radius about the El Mayor-Cucapah epicenter. We collectively describe the coseismic and postseismic displacements resulting from the El Mayor-Cucapah earthquake as  $u_{\text{post}}(t)$ . We consider the GPS position time series  $u_{\text{obs}}(t)$  to be the combination of  $u_{\text{post}}(t)$ , secular tectonic deformation, annual and semi-annual oscillations, and coseismic offsets from significant earthquakes over the time span of this study. The June 14, 2010, Mw=5.8 Ocotillo earthquake and the Brawley swarm, which included an Mw=5.5 and an Mw=5.4 event on August 26, 2012, (Figure 1) are the only earthquakes that produced noticeable displacements in any of the time series. We treat the displacements resulting from the Brawley swarm as a single event because the daily solutions provided by UNAVCO cannot resolve the separate events. Although the Ocotillo earthquake had its own series of aftershocks [Hauksson *et al.*, 2011], neither the Ocotillo earthquake nor the Brawley swarm produced detectable postseismic deformation. We model displacements resulting from these events with only a Heaviside function,  $H(t)$ , describing the coseismic offsets. We then model  $u_{\text{obs}}(t)$  as

$$u_{\text{obs}}(t) = u_{\text{pred}}(t) + \epsilon, \quad (1)$$

where

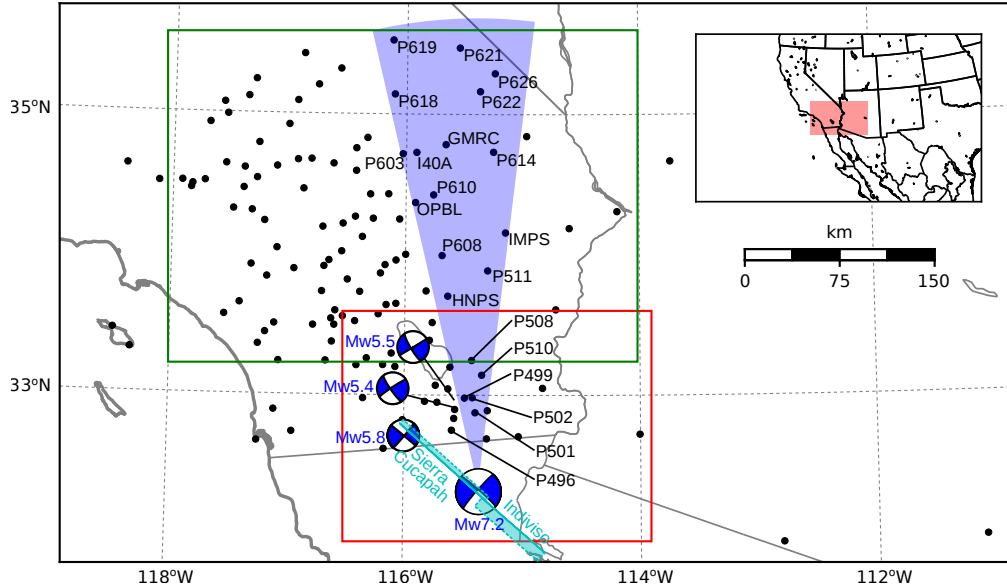


**Figure 1.** Map of the region considered in this study. The large focal mechanism is for the El Mayor-Cucapah earthquake, and the three small focal mechanisms are for the Ocotillo earthquake and the two main shocks during the Brawley swarm. The black dots indicate the locations of GPS stations used in this study. The fault geometry used in this study is shown in cyan where dashed lines indicate buried edges of the fault segments. The green and red boxes demarcate the extent of the near-field and far-field maps (Figures 4 and 5). Stations inside the blue sector, which highlights the area within  $10^{\circ}$  of the El Mayor-Cucapah P axis, are used in Figures 7 and 10.

$$u_{\text{pred}}(t) = u_{\text{post}}(t)H(t - t_{\text{emc}}) + c_0 + c_1t + \\ c_2 \sin(2\pi t) + c_3 \cos(2\pi t) + c_4 \sin(4\pi t) + c_5 \cos(4\pi t) + \\ c_6 H(t - t_{\text{oc}}) + c_7 H(t - t_{\text{bs}}). \quad (2)$$

In the above equations,  $t_{\text{emc}}$ ,  $t_{\text{oc}}$  and  $t_{\text{bs}}$  are the times of the El Mayor-Cucapah earthquake, Ocotillo earthquake, and the Brawley swarm, respectively,  $c_0$  through  $c_7$  are unknown coefficients, and  $\epsilon$  is the observation noise. We only estimate jumps associated with the Ocotillo earthquake and Brawley swarm for stations within 40 km of their epicenters.

Stations which recorded displacements that clearly cannot be described by the aforementioned processes are not included in our analysis. This includes stations in the Los Angeles basin, where anthropogenic deformation can be larger than the postseismic signal that we are trying to estimate [Bawden *et al.*, 2001; Argus *et al.*, 2005]. In order to ensure an accurate estimation of the secular deformation, we only use stations that were installed at least six months prior to El Mayor-Cucapah earthquake. Several GPS stations were installed after the El Mayor-Cucapah earthquake to improve the spatial resolution of postseismic deformation [Spinler *et al.*, 2015]. Although it would be possible to subtract secular velocities derived from elastic block models [e.g. Meade and Hager, 2005] from velocities recorded at the newly installed stations to get an estimate of postseismic velocities, we do not do so here. We use coseismic and postseismic displacements, rather than velocities, in our inverse method described in Section 3. We use displacements because estimating velocities from an already noisy displacement time series can introduce significant uncertainties depending on exactly how the estimation is done. This choice prevents us from using the newly installed stations in Baja California for our analysis.

The October 16, 1999, Mw=7.1 Hector Mine earthquake, which occurred  $\sim$ 270 km north of the El Mayor-Cucapah epicenter, produced transient postseismic deformation which we do not wish to model, either mechanically or through empirical line fitting. We thus restrict our analysis to deformation observed six years after the Hector Mine earthquake, which is when postseismic velocities at sites proximal to the Hector Mine epicenter are approximately constant [Savage and Svare, 2009]. When appraising our model fit in Section 3, we see some systematic residuals in the vicinity of the Hector Mine epicenter, which may be the result of errors in the assumption that the trend in Hector Mine postseismic deformation is linear after six years.

Studies of postseismic deformation typically assume a parametric form for  $u_{\text{post}}(t)$ , such as one with a logarithmic or exponential time dependence [e.g. Savage *et al.*, 2005]. However, by assuming a logarithmic or exponential form of  $u_{\text{post}}(t)$  we run the risk of over fitting the GPS time series and inferring a non-existent postseismic signal. We therefore do not assume any parametric form for  $u_{\text{post}}(t)$  and rather treat it as integrated Brownian motion, so that

$$\dot{u}_{\text{post}}(t) = \sigma^2 \int_0^t w(s) ds, \quad (3)$$

where  $w(t)$  is white noise and the variance of  $\dot{u}_{\text{post}}(t)$  increases linearly with time by a factor of  $\sigma^2$ . We use a Kalman filtering approach to estimate  $u_{\text{post}}(t)$  and the unknown parameters in eq. (2). In the context of Kalman filtering, our time varying state vector is

$$\mathbf{X}(t) = [u_{\text{post}}(t), \dot{u}_{\text{post}}(t), c_0, \dots, c_7] \quad (4)$$

and eq. (2) is the observation function which maps the state vector to the GPS observations. We initiate the Kalman filter by assuming a prior estimate of  $\mathbf{X}(t)$  at the first time epoch, denoted  $\mathbf{X}_{1|0}$ , which has a sufficiently large covariance, denoted  $\Sigma_{1|0}$ , to effectively make our prior uninformed. For each time epoch  $t_i$ , Bayesian linear regression is used to incorporate GPS derived estimates of displacement with our prior estimate of the state  $\mathbf{X}_{i|i-1}$  to form a posterior estimate of the state  $\mathbf{X}_{i|i}$ , which has covariance  $\Sigma_{i|i}$ . We then use the posterior estimate of the state at time  $t_i$  to form a prior estimate of the state at time  $t_{i+1}$  through the transition function

$$\mathbf{X}_{i+1|i} = \mathbf{F}_{i+1} \mathbf{X}_{i|i} + \delta_{i+1}, \quad (5)$$

where

$$\mathbf{F}_{i+1} = \begin{bmatrix} 1 & (t_{i+1} - t_i) & \mathbf{0} \\ 0 & 1 & \mathbf{0} \\ \mathbf{0} & \mathbf{0} & \mathbf{I} \end{bmatrix} \quad (6)$$

and  $\delta_{i+1}$  is the process noise, which has zero mean and covariance described by

$$\mathbf{Q}_{i+1} = \sigma^2 \begin{bmatrix} \frac{(t_{i+1}-t_i)^3}{3} & \frac{(t_{i+1}-t_i)^2}{2} & \mathbf{0} \\ \frac{(t_{i+1}-t_i)^2}{2} & (t_{i+1} - t_i) & \mathbf{0} \\ \mathbf{0} & \mathbf{0} & \mathbf{0} \end{bmatrix}. \quad (7)$$

The covariance of the new prior state,  $\mathbf{X}_{i+1|i}$ , is then described by

$$\Sigma_{i+1|i} = \mathbf{F}_{i+1} \Sigma_{i|i} \mathbf{F}_{i+1}^T + \mathbf{Q}_{i+1}. \quad (8)$$

This process is repeated for each of the  $N$  time epochs at which point we use Rauch-Tung-Striebel smoothing [Rauch *et al.*, 1965] to find  $\mathbf{X}_{i|N}$ , which is an estimate of the state at time  $t_i$  that incorporates GPS observation for all  $N$  time epochs. Our final estimates of  $u_{\text{post}}(t)$

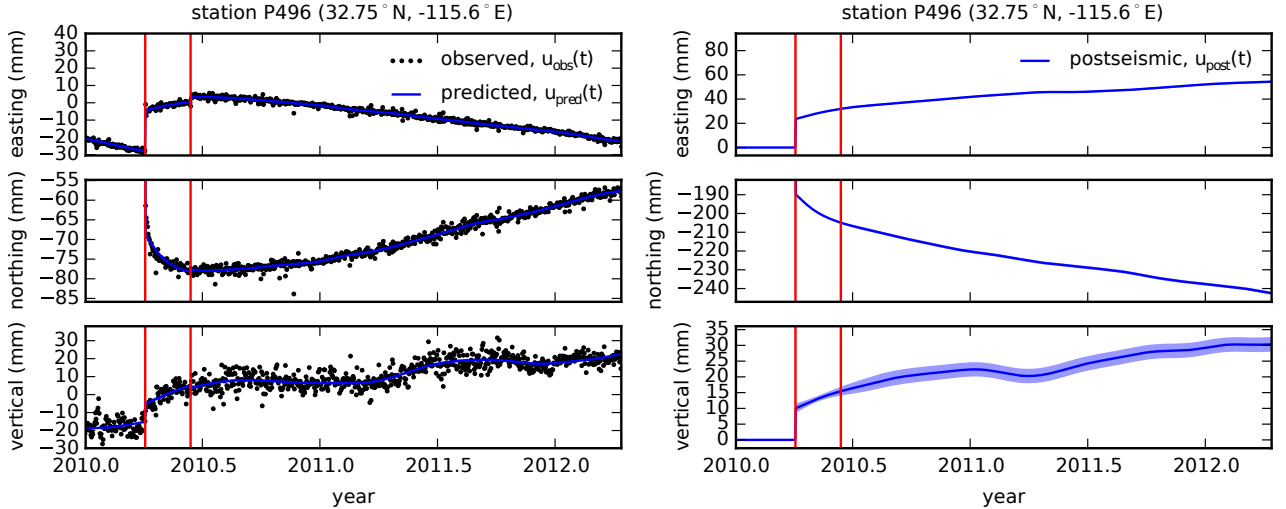


**Figure 2.** Left panels show GPS time series from UNAVCO (black) and the predicted displacement (blue) from eq. (2) for a near-field station. Red lines indicate the times of the El Mayor-Cucapah and Ocotillo earthquake. The right panels show estimated coseismic and postseismic displacements  $u_{\text{post}}$  which are extracted from the predicted displacements. The 68% confidence interval is shown in light blue.

are used in subsequent analysis, while the remaining components of the state vector are considered nuisance parameters. In the interests of computational tractability, we down sample our smoothed time series from daily solutions down to weekly solutions.

The smoothness of  $u_{\text{post}}(t)$  is controlled by the chosen value of  $\sigma^2$ , which describes how rapidly we expect postseismic displacements to vary over time. Setting  $\sigma^2$  equal to zero will effectively result in modeling  $u_{\text{post}}(t)$  as a straight line which is insufficient to describe the expected transient behavior in postseismic deformation. The other end member, where  $\sigma^2$  is infinitely large, will result in  $u_{\text{pred}}(t)$  over fitting the data. While one can use a maximum likelihood based approach for picking  $\sigma^2$  [e.g. Segall and Mathews, 1997], we instead take a subjective approach and choose a value for  $\sigma^2$  that is just large enough to faithfully describe the observed deformation at the most near-field station in our study, P496, which exhibits the most rapid changes in velocity. This ensures that  $\sigma^2$  will be sufficiently large so that our estimate of  $u_{\text{post}}(t)$  does not smooth out potentially valuable postseismic signal at the remaining stations. We find that using  $\sigma^2 = 0.05 \text{ m}^2/\text{yr}^3$  adequately describe all but the first week of postseismic deformation at station P496, which gets incorporated into our estimate of coseismic displacements (Figure 2). We assume that the first week of deformation is overwhelmingly the result of afterslip and this afterslip is lumped into our estimates of coseismic slip. Freed *et al.* [2007] noted that postseismic deformation can be observed at distances greater than 200 km from the Hector Mine earthquake and, after filtering the time series for stations up to 400 km from the El Mayor-Cucapah epicenter, we also clearly see far reaching postseismic transient deformation (Figure 3).

It is important to note that the shown uncertainties in  $u_{\text{post}}(t)$  do not account for the non-negligible epistemic uncertainty in eq. (2). For example, we assume a constant rate of secular deformation, which appears to be an appropriate approximation for all but perhaps the stations closest to the Hector Mine epicenter, as noted above. Also, our model for seasonal deformation in eq. (2) assumes a constant amplitude over time, which means that any yearly variability in the climatic conditions could introduce systematic residuals [Davis *et al.*, 2012]. Indeed, it would be more appropriate to consider the seasonal amplitudes  $c_2-c_5$  in eq. (2) as stochastic variables [Murray and Segall, 2005]. By using constant seasonal amplitudes, our es-

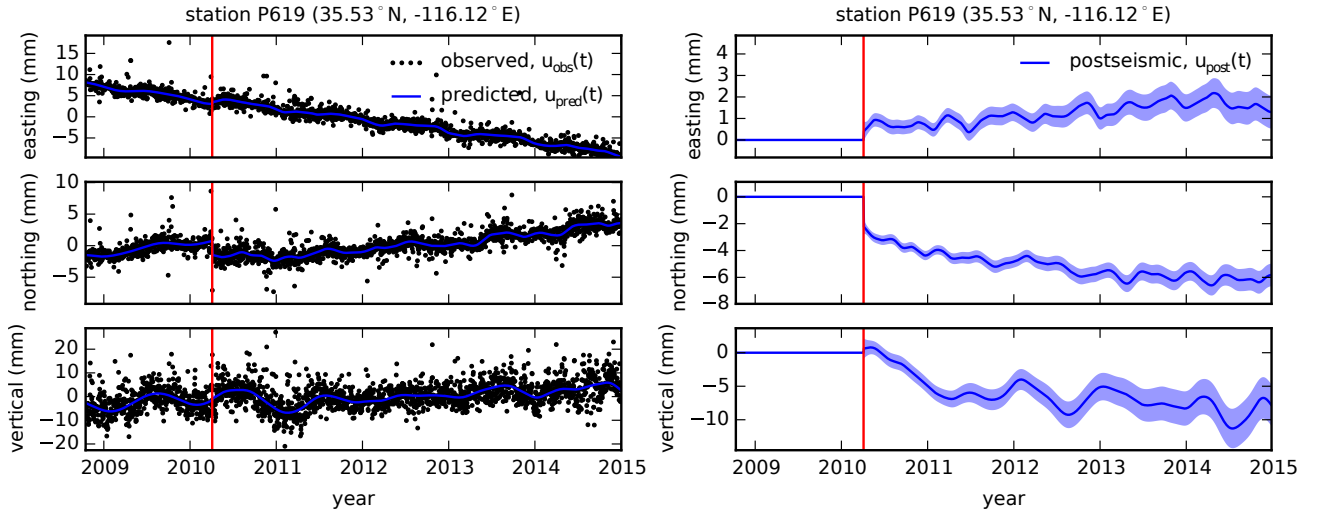


**Figure 3.** same as Figure 2 but for a far-field station.

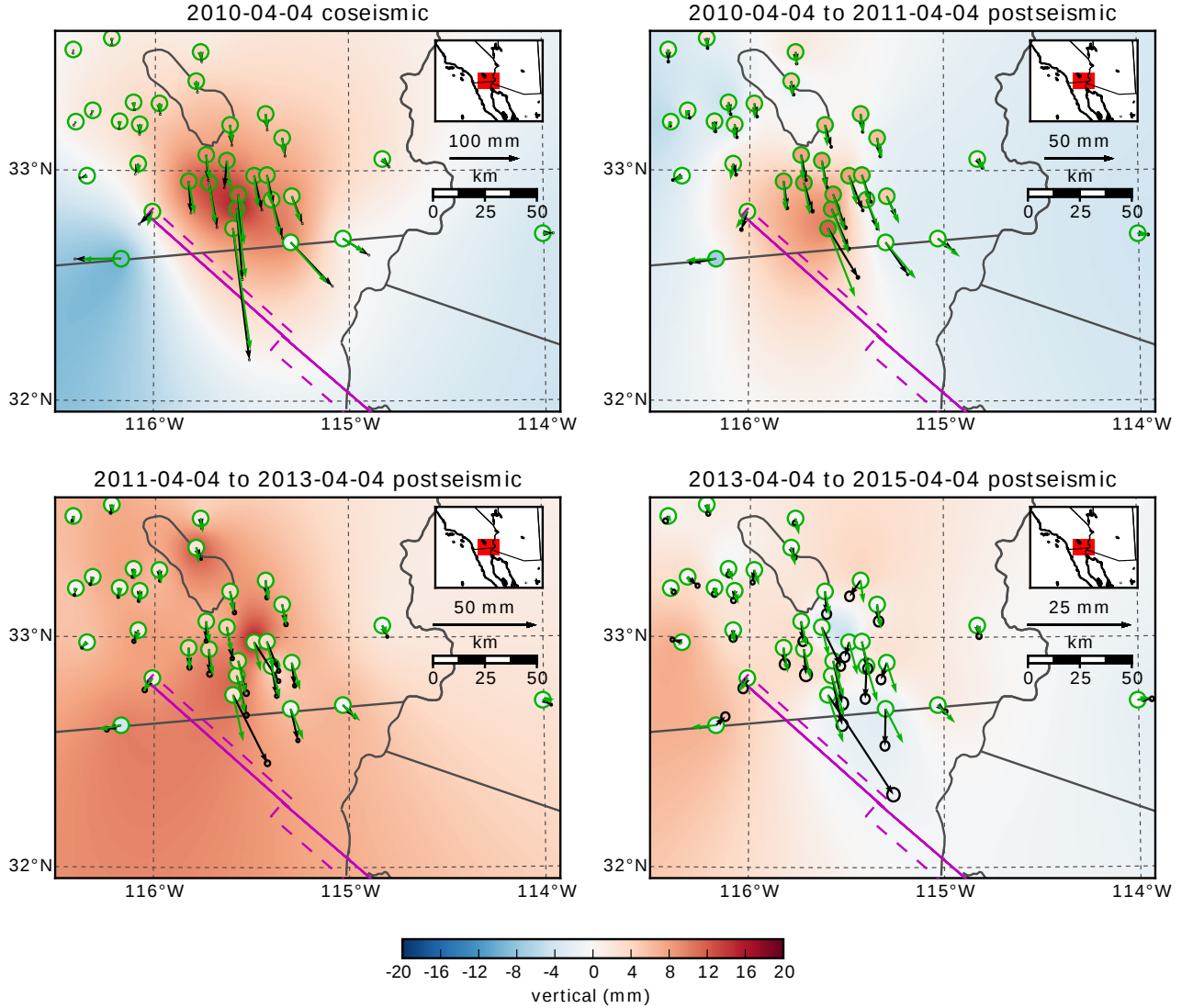
timate of  $u_{\text{post}}(t)$  seems to describe some of the unmodeled annual and semi-annual oscillations (e.g. Figure 3).

We show in Figures 4 and 5 the near and far-field postseismic displacements accumulated over the time intervals 0-1 years, 1-3 years, and 3-5 years, as well as the coseismic displacements. Stations at epicentral distances beyond  $\sim 200$  km have an elevated rate of deformation for the first three years following the earthquake. This far-field deformation has a southward trend along the direction of the El Mayor-Cucapah P axis and a similar eastward trend can be seen in the few far-field stations in Arizona, located along the T axis. After three years, the trend in far-field postseismic deformation is barely perceptible. Most far-field stations display an initial subsidence for the first year after the El Mayor-Cucapah earthquake followed by continued uplift. This trend in vertical deformation can be observed in all three of the quadrants where postseismic data is available, which means that the vertical deformation does not exhibit an anti-symmetric quadrant pattern, as would be expected for postseismic processes. Although we use vertical deformation in our analysis in Section 3, we do not put an emphasis on trying to describe the vertical deformation as it likely does not have postseismic origins.

The near-field postseismic deformation is notably sustained when compared to the far-field deformation. Namely, the station in this study which is closest to the El Mayor-Cucapah epicenter, P496, has a steady postseismic trend of  $\sim 1.5$  cm/yr to the south after about one year. Vertical postseismic deformation in the near-field does display a quadrant pattern which is consistent with the coseismic vertical deformation, suggesting that it is resulting from postseismic processes. However, the vertical postseismic signal is only apparent for the first year after the earthquake (Figure 4). As with the far-field deformation, there is a general trend of uplift in the near-field after about one year.

### 3 Postseismic Modeling

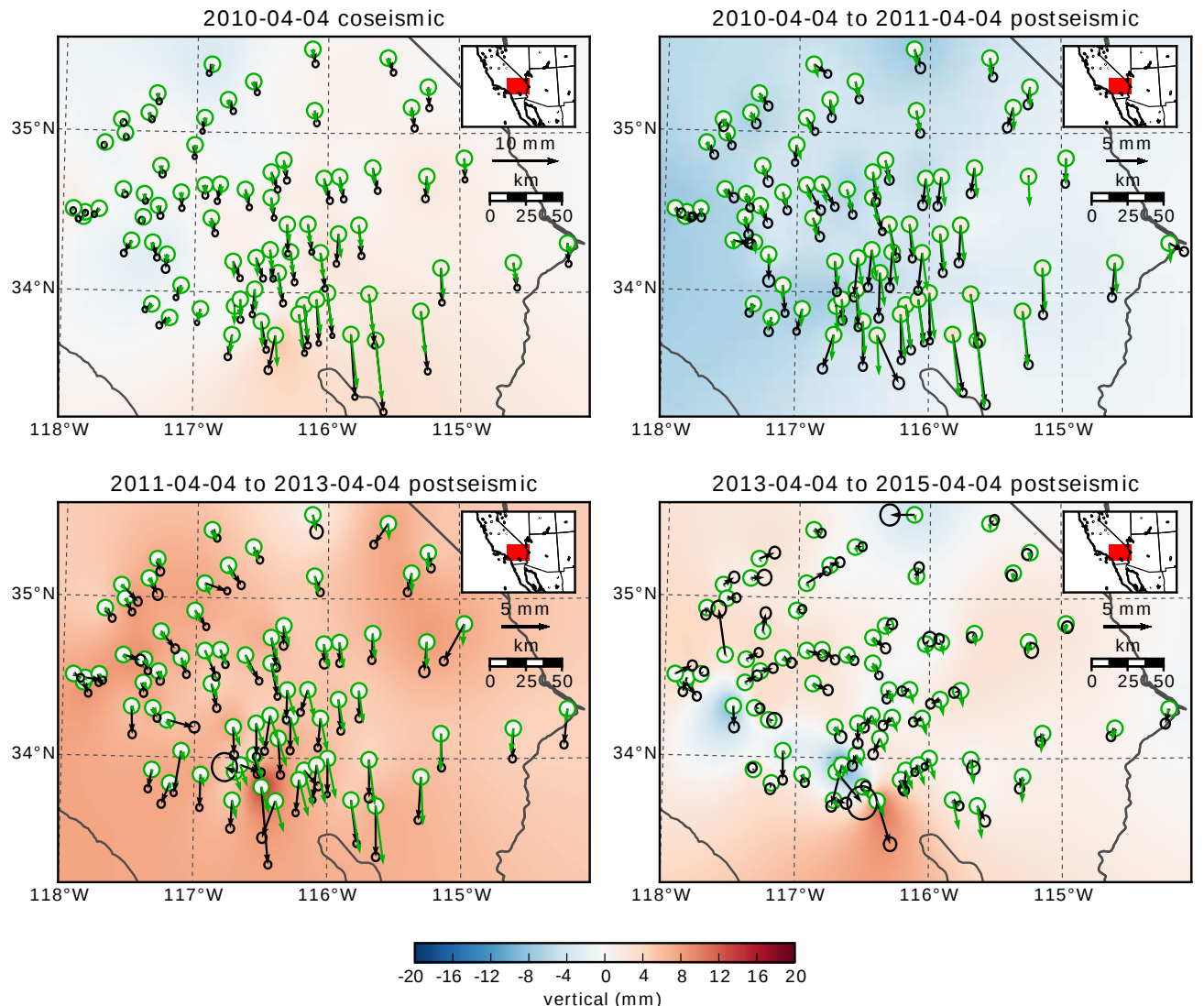
We seek to find the mechanisms driving five years of postseismic deformation following the El Mayor-Cucapah earthquake and we consider afterslip and viscoelastic relaxation as candidate mechanisms. Poroelastic rebound has also been used to model postseismic deformation [e.g. Jónsson *et al.*, 2003]; however, Gonzalez-Ortega *et al.* [2014] found that poroelastic rebound is unlikely to be a significant contributor to postseismic deformation following



216 **Figure 4.** Near-field coseismic and cumulative postseismic displacements over the indicated time periods  
 217 (black) as well as predicted displacements for our preferred model from Section 3.3 (green). Observed verti-  
 218 cal deformation is shown as an interpolated field and predicted vertical displacements are shown within the  
 219 circles at the base of each vector. Note that the interpolant is not well constrained in Mexico where there is no  
 220 data available.

depth (km)	$\lambda$ (GPa)	$\mu$ (GPa)	$\eta_{\text{eff}}$ ( $10^{18}$ Pa s)	$\mu_k/\mu$
0-5	24.0	24.0	-	-
5-15	35.0	35.0	-	-
15-30	42.0	42.0	44.3	0.0
30-60	61.0	61.0	5.91	0.375
60-90	61.0	61.0	1.99	0.375
90-120	61.0	61.0	1.31	0.375
120-150	61.0	61.0	1.10	0.375
150-∞	61.0	61.0	1.07	0.375

231 **Table 1.** Assumed and estimated material properties.  $\lambda$  and  $\mu$  are assumed known *a priori* and are based  
 232 on the values used for the coseismic model by Wei *et al.* [2011b]. The values for  $\eta_{\text{eff}}$  are estimated in Section  
 233 3.2, and  $\mu_k/\mu$  are the optimal shear moduli ratios found in Section 3.3 for a Zener rheology upper mantle.

**Figure 5.** Same as Figure 4 but for far-field stations.

239 the El Mayor-Cucapah earthquake. Furthermore, we consider stations which are sufficiently  
240 far away from the main rupture that poroelastic rebound should be insignificant.

241 We estimate coseismic and time-dependent postseismic fault slip, both of which are assumed  
242 to occur on a fault geometry modified from *Wei et al.* [2011b]. Field studies [*Fletcher et al.*,  
243 2014] and LIDAR observations [*Oskin et al.*, 2012] have revealed a significantly more complicated  
244 fault geometry than what was inferred by *Wei et al.* [2011b], especially within the Sierra Cucapah.  
245 However, we find that a relatively simple coseismic fault geometry based on [*Wei et al.*, 2011b] is adequate  
246 because most of the stations used in this study are sufficiently far from the El Mayor-Cucapah rupture  
247 zone that they are insensitive to the details in the fault geometry found by *Fletcher et al.* [2014] and  
248 *Oskin et al.* [2012]. The fault geometry used in this study (Figure 1) consists of the two main fault  
249 segments inferred by *Wei et al.* [2011b], where the northern segment runs through the Sierra Cucapah up to  
250 the US-Mexico border and the southern segment is the Indiviso fault which extends down to the Gulf of California.  
251 Both segments extend from the surface to 15 km depth. We extend the northern segment by 40 km  
252 to the north-west, motivated by the clustering of aftershocks on the northern tip of the coseis-  
253 mic rupture zone [*Hauksson et al.*, 2011; *Kroll et al.*, 2013]. This extended fault segment was  
254 also found to be necessary by *Rollins et al.* [2015] and *Pollitz et al.* [2012] in order to describe  
255 the postseismic deformation.

### 257 3.1 Elastic Postseismic Inversion

258 We consider a variety of rheologic models for the lower crust and upper mantle. The  
259 simplest rheologic model is to consider them to be effectively elastic and isotropic. In such  
260 case, the rheologic parameters consist of the Lamé parameters,  $\lambda$  and  $\mu$ , which are reasonably  
261 well known and we use the same values used by *Wei et al.* [2011b] throughout this paper (Ta-  
262 ble 1). The only unknown is the distribution of fault slip, which can be easily estimated from  
263 postseismic deformation through linear least squares. Using a subset of the GPS stations con-  
264 sidered in this study, *Rollins et al.* [2015] found that three years of postseismic deformation  
265 following the El Mayor-Cucapah earthquake can be explained with afterslip on the coseismic  
266 fault plane without requiring any viscoelastic relaxation. We also perform an elastic slip in-  
267 version, but we use GPS stations within a larger radius about the El Mayor-Cucapah epicen-  
268 ter (400 km instead of  $\sim$ 200 km). Our forward problem describing predicted postseismic de-  
269 formation  $u_{\text{pred}}$  in terms of time dependent fault slip,  $s$ , is

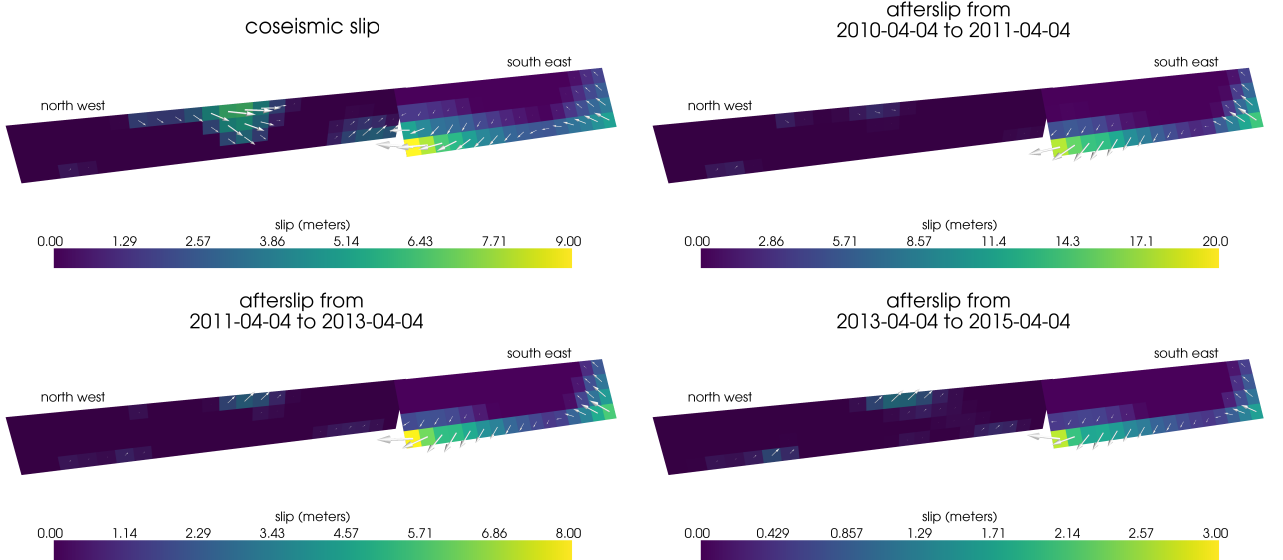
$$270 u_{\text{pred}}(x, t) = \int_F s(\xi, t)g(x, \xi)d\xi, \quad (9)$$

271 where  $F$  denotes the fault and  $g(x, \xi)$  is the elastic Green's function describing displacement  
272 at surface position  $x$  resulting from slip at  $\xi$  on the fault. We estimate coseismic slip and the  
273 rate of afterslip over the time intervals 0.0-0.125, 0.125-0.25, 0.5-1.0, 1.0-2.0, 2.0-3.0, 3.0-4.0,  
274 and 4.0-5.0 years after the earthquake. Each fault segment is discretized into roughly 4 km  
275 by 4 km patches and we estimate a strike-slip and dip component of slip for each patch. We  
276 impose that the direction of slip and slip rate are within  $45^\circ$  of right-lateral. We also add zeroth-  
277 order Tikhonov regularization so that our solution for  $s$  satisfies

$$278 \min_s \left( \left\| \frac{u_{\text{pred}}(s) - u_{\text{post}}}{\sigma_{\text{post}}} \right\|_2^2 + \lambda_s \|s\|_2^2 \right), \quad (10)$$

279 where  $\sigma_{\text{post}}$  is the uncertainty on postseismic displacements and  $\lambda_s$  is a penalty parameter which  
280 is chosen with a trade-off curve. We use Pylith [*Aagaard et al.*, 2013] to compute the Green's  
281 functions for this inversion as well as for the remaining inversions in this paper.

282 Our coseismic slip and afterslip solutions are shown in Figure 6. As with *Rollins et al.*  
283 [2015], we find that a large amount of afterslip on the southern fault segment is required to  
284 explain the observations. The potency of our inferred coseismic slip is  $3.2 \times 10^9 \text{ m}^3$ , equiv-  
285 alent to a Mw=7.28 earthquake when assuming a shear modulus of 32 GPa. The potency of



296 **Figure 6.** Coseismic slip and cumulative afterslip over the indicated intervals for the elastic model from  
297 Section 3.1. Color indicates the magnitude of slip while arrows indicate the motion of the hanging wall.

284 our inferred cumulative five years of afterslip is  $6.1 \times 10^9 \text{ m}^3$ , equivalent to a  $M_w=7.46$  earth-  
285 quake, which is unrealistically large if we consider afterslip to be driven by coseismically in-  
286 duced stresses. Figure 7 shows the time series for the observed and predicted postseismic dis-  
287 placements at stations along the El Mayor-Cucapah P axis. We show the radial component of  
288 displacements with respect to the El Mayor-Cucapah epicenter and we also rescale the dis-  
289 placements so that the difference between the minimum and maximum observed displacements  
290 are the same for each station. Our elastic slip model accurately describes near-field postseis-  
291 mic deformation and systematically underestimates postseismic deformation at epicentral dis-  
292 tances  $\gtrsim 150 \text{ km}$ . When the fault segments used in the inversion are extended down to 30 km  
293 depth, rather than 15 km, the systematic far-field residuals are smaller but remain apparent.  
294 Because an elastic model requires an unrealistic amount of afterslip and is unable to predict  
295 far-field deformation, we move on to consider viscoelastic models in the next section.

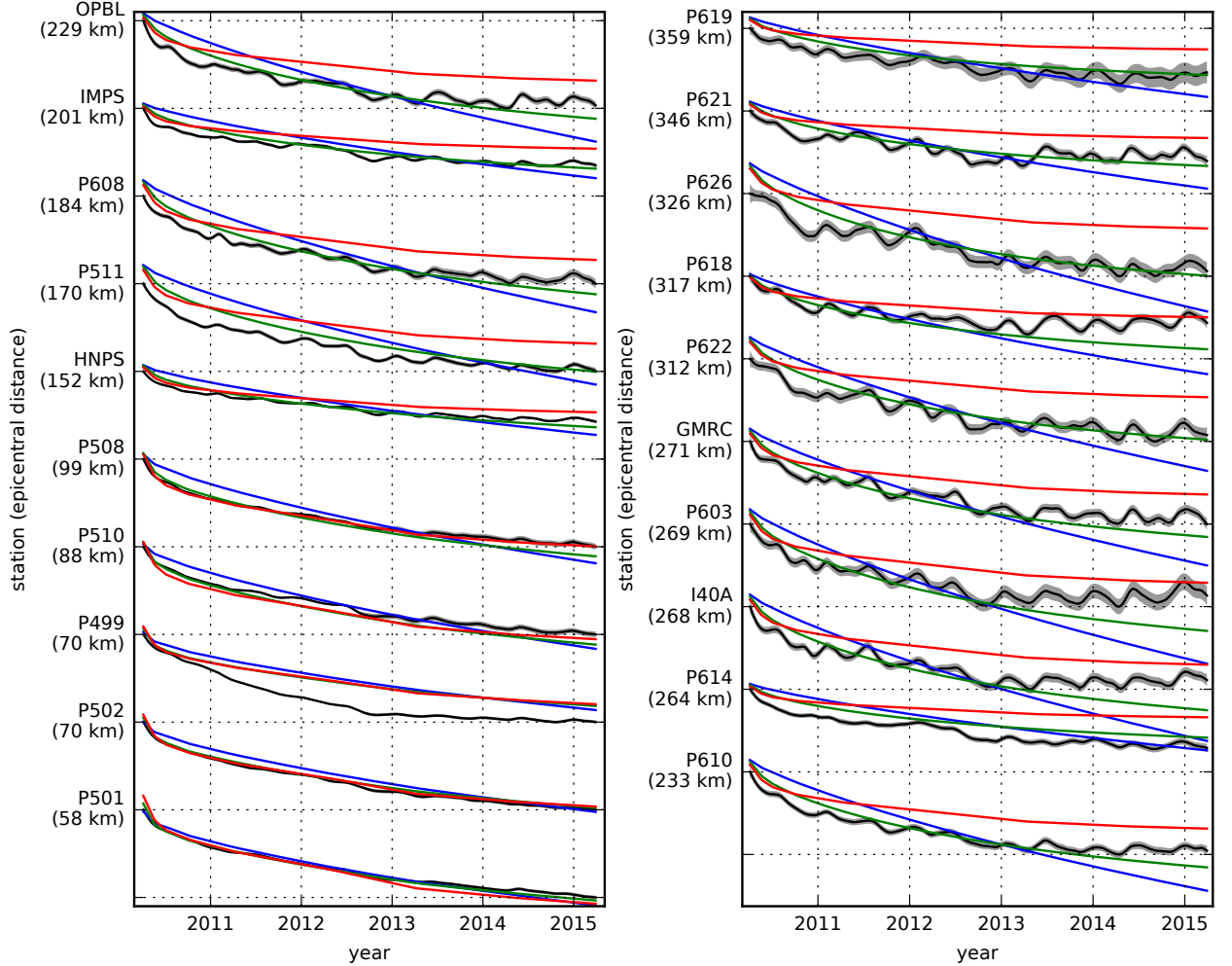
### 307 3.2 Early Postseismic Inversion

308 For any linear viscoelastic rheology of the crust and mantle, postseismic displacements  
309 resulting from time dependent fault slip can be described as

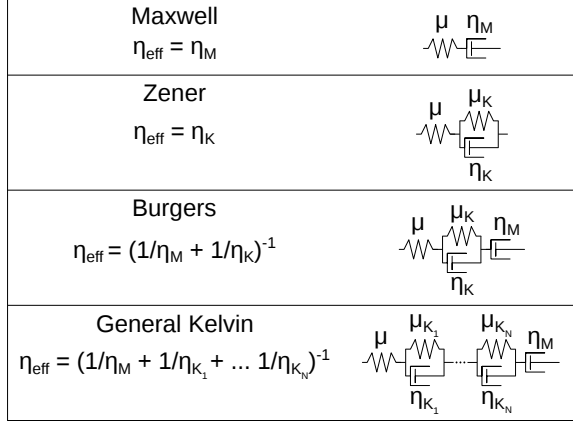
$$u_{\text{pred}}(x, t) = \int_F s(\xi, t) g(x, \xi) d\xi + \int_0^t \int_F s(\xi, \tau) f(t - \tau, x, \xi) d\xi d\tau, \quad (11)$$

310 where  $f(t, x, \xi)$  describes the time-dependent velocity at  $x$  resulting from viscoelastic relax-  
311 ation of stresses induced by slip at  $\xi$ .  $f$  is a function of  $\lambda$ ,  $\mu$ , and any additional rheologic pa-  
312 rameters controlling the viscoelastic response, which are generally not well known. Schematic  
313 representations of the viscoelastic rheologic models considered in this study are shown in Fig-  
314 ure 8. We discuss these rheologic models and their use in geophysical studies in Section 4.

317 In order to greatly simplify the inverse problem, we use the method described in *Hines*  
318 and *Hetland* [2016] to constrain an initial effective viscosity structure from the early postseis-  
319 mic deformation. Our method utilizes the fact that coseismic stresses throughout the crust and  
320 upper mantle depend on the instantaneous elastic parameters and are independent of the vis-



298 **Figure 7.** Scaled radial component of postseismic displacements. Downward motion indicates that the  
 299 station is moving toward the El Mayor-Cucapah epicenter. Displacement time series are scaled so that the  
 300 minimum and maximum observed values lie on the grid lines. The observed postseismic displacements,  $u_{\text{obs}}$   
 301 are shown in black with gray indicating the 68% confidence interval. The displacements predicted by the best  
 302 fitting elastic model  $u_{\text{pred}}$  are shown in red. The blue and green lines are the predicted postseismic displace-  
 303 ments for the models discussed in Section 3.3. The blue lines show the predicted displacements for the model  
 304 with a Maxwell viscoelastic lower crust and upper mantle. The green line shows the predicted displacements  
 305 for the model with a Maxwell viscoelastic lower crust and a Zener viscoelastic upper mantle (green). The  
 306 effective viscosities are the same for both models and are shown in Figure 11.



315 **Figure 8.** Schematic illustration of the rheologic models considered in this paper as well as their effective  
 316 viscosities.

321 coelastic parameters which we wish to estimate. Immediately following an earthquake, each  
 322 parcel will have a strain rate that is proportional to the coseismic stress and inversely propor-  
 323 tional to the parcel's effective viscosity,  $\eta_{\text{eff}}$ . Using one-dimensional viscoelastic models, we  
 324 define the effective viscosity as

$$\eta_{\text{eff}} = \left. \frac{\sigma}{\dot{\varepsilon}} \right|_{t=0}, \quad (12)$$

325 where  $\sigma$  is an applied stress at  $t = 0$  and  $\dot{\varepsilon}$  is the resulting strain rate. Figure 8 shows how  
 326  $\eta_{\text{eff}}$  relates to the parameters for various linear viscoelastic rheologies. We can deduce that the  
 327 initial rate of surface deformation resulting from viscoelastic relaxation is a summation of the  
 328 surface deformation resulting from relaxation in each parcel, scaled by the reciprocal of the  
 329 parcel's effective viscosity. That is to say

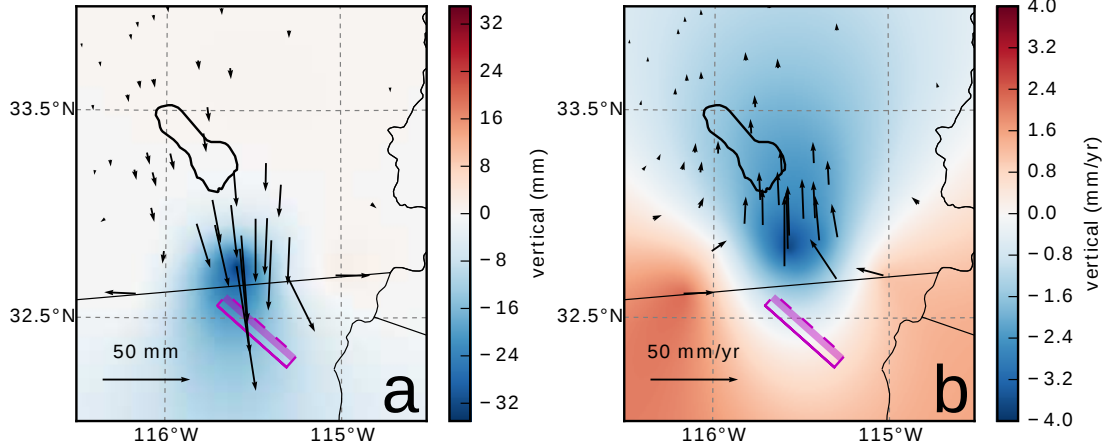
$$f(0, x, \xi) = \int_L \frac{h(x, \xi, \zeta)}{\eta_{\text{eff}}(\zeta)} d\zeta, \quad (13)$$

330 where  $L$  denotes the crust and mantle and  $h(x, \xi, \zeta)$  describes the initial rate of deformation  
 331 resulting from viscoelastic relaxation at  $\zeta$  induced by slip at  $\xi$ . We can combine eq. (13) with  
 332 eq. (11) to get a first order approximation for early postseismic deformation,

$$u_{\text{pred}}(x, t) \approx \int_F s(\xi, t) g(x, \xi) d\xi + \int_0^t \int_F \int_L \frac{s(\tau, \xi)}{\eta_{\text{eff}}(\zeta)} h(x, \xi, \zeta) d\zeta d\xi d\tau, \quad (14)$$

333 which is valid for as long as the rate of deformation resulting from viscoelastic relaxation is  
 334 approximately constant. Although eq. (14) may only be valid for a short portion of the post-  
 335 seismic period, its utility becomes apparent when noting that  $g$  and  $h$  are only functions of  
 336 the fault geometry and instantaneous elastic properties,  $\lambda$  and  $\mu$ , and thus  $g$  and  $h$  can be com-  
 337 puted numerically as a preprocessing step. The forward problem in eq. (14) can then be rapidly  
 338 evaluated for any realization of  $s$  and  $\eta_{\text{eff}}$ . This is in contrast to evaluating the full forward  
 339 problem, eq. (11), numerically for each realization of  $s$  and the unknown rheologic proper-  
 340 ties.

341 Details on how eq. (14) is used to estimate  $s$  and  $\eta_{\text{eff}}$  from postseismic deformation can  
 342 be found in *Hines and Hetland* [2016]. A non-linear Kalman filter based inverse method can  
 343 also be used to estimate  $s$  and  $\eta_{\text{eff}}$  in a manner akin to *Segall and Mathews* [1997] or *McGuire*  
 344 and *Segall* [2003], in which we would not have to explicitly impose a time dependent parametriza-  
 345 tion of  $s$ . We have thoroughly explored Kalman filter based approaches, but we ultimately pre-



371 **Figure 9.** Displacements resulting from fault slip at lower crustal depths (a), and initial velocities resulting  
 372 from subsequent relaxation of a viscoelastic lower crust (b). The fault segment dips  $75^\circ$  to the north-east and  
 373 its surface projection is outlined in magenta. The highlighted area on the fault extends from 15 to 30 km depth  
 374 and indicates where 1 meter of right-lateral slip was imposed. The elastic properties of the crust and mantle  
 375 are the same as in Table 3, and  $\eta_{\text{eff}}$  is  $10^{18}$  Pa s in the lower crust. Vertical displacements are interpolated  
 376 between station locations.

346 for the method described in *Hines and Hetland* [2016] because of its relative simplicity. More-  
 347 over, we believe the piecewise continuous representation of slip with respect to time to be suf-  
 348 ficiently general for the resolving power of these GPS data.

349 We estimate coseismic slip and afterslip with the same spatial and temporal discretiza-  
 350 tion as in Section 3.1. Simultaneously, we estimate  $\eta_{\text{eff}}$  within six vertically stratified layers  
 351 which have depths ranging from 15–30 km, 30–60 km, 60–90 km, 90–120 km, 120–150 km,  
 352 as well as from 150 km to the bottom of our numerical model domain at 800 km. We again  
 353 restrict fault slip to occur between 0 and 15 km depth, which is done in order to help elim-  
 354 inate inevitable non-uniqueness in the inversion. It has long been recognized that fault slip at  
 355 sufficiently great depths can produce surface deformation that is indistinguishable from vis-  
 356 coelastic relaxation, at least in two-dimensional earthquake models [Savage, 1990]. Addition-  
 357 ally, we note that when simultaneously estimating both afterslip and viscosity in the lower crust,  
 358 the inverse problem becomes particularly ill-posed. This ill-posedness is illustrated in Figure  
 359 9, which shows the displacements resulting from a meter of slip on a fault extending from 15  
 360 to 30 km depth and the initial velocity resulting from subsequent viscoelastic relaxation in the  
 361 lower crust, which is given a viscosity of  $10^{18}$  Pa s. In this demonstration, the viscoelastic re-  
 362 laxation is entirely driven by the fault slip in the lower crust. The horizontal displacements  
 363 from fault slip are in the opposite direction as the displacements resulting from viscoelastic  
 364 relaxation. This means that surface displacements resulting from afterslip at lower crustal depths  
 365 can be cancelled out, at least partially, by a low viscosity lower crust. We eliminate this null  
 366 space by allowing only one mechanism in the lower crust, which we choose to be viscoelas-  
 367 tic relaxation. This is not to say that we do not believe deep afterslip to be a possibility; rather,  
 368 we restrict slip to seismogenic depths as a modeling necessity. Although, it has been noted  
 369 that the pattern of vertical postseismic deformation following the El Mayor-Cucphuong earthquake  
 370 indicates that a significant amount of afterslip must be shallow [Rollins et al., 2015].

377 We must determine at which point the early postseismic approximation breaks down, which  
 378 we will denote as  $t_{\text{bd}}$ . As noted, eq. (14) is valid for approximately as long as the rate of de-  
 379 formation resulting from viscoelastic relaxation is approximately constant. We can almost cer-  
 380 tainly assume that deformation at the most far-field stations, which are  $\sim 400$  km away from

the El Mayor-Cucapah epicenter, is the result of viscoelastic relaxation. The approximation should then be valid for as long as a linear trend adequately approximates the far-field deformation. Using this logic, it would appear that  $t_{bd}$  is about one year after the El Mayor-Cucapah earthquake. Another way to determine  $t_{bd}$  is to find the best fitting prediction of eq. (14) to observed deformation using increasing durations of the postseismic time series.  $t_{bd}$  should be the point when eq. (14) is no longer capable of describing the observed deformation without incurring systematic misfits. When using eq. (14) to fit the entire five years of postseismic displacements, we see that the near-field displacements (e.g., station P501) are accurately predicted. When looking at displacements in the far-field (e.g., station P621), we see that eq. (14) overestimates the rate of deformation in the later postseismic period and underestimates the rate of deformation in the early period (Figure 10). Due to the low signal-to-noise ratios for far-field stations, it is difficult to determine at what point eq. (14) is no longer able to predict the observed displacements; however, we settle on  $t_{bd} = 0.8$  years after the earthquake, while acknowledging that the choice is subjective. As noted in *Hines and Hetland* [2016], overestimating  $t_{bd}$  will result in a bias towards overestimating  $\eta_{eff}$ , while picking a  $t_{bd}$  which is too low will not necessarily result in a biased estimate of  $\eta_{eff}$ , although the uncertainties would be larger. We can then consider inferences of  $\eta_{eff}$  to be an upper bound on the viscosity needed to describe the far-field rate of deformation during the first 0.8 years of postseismic deformation.

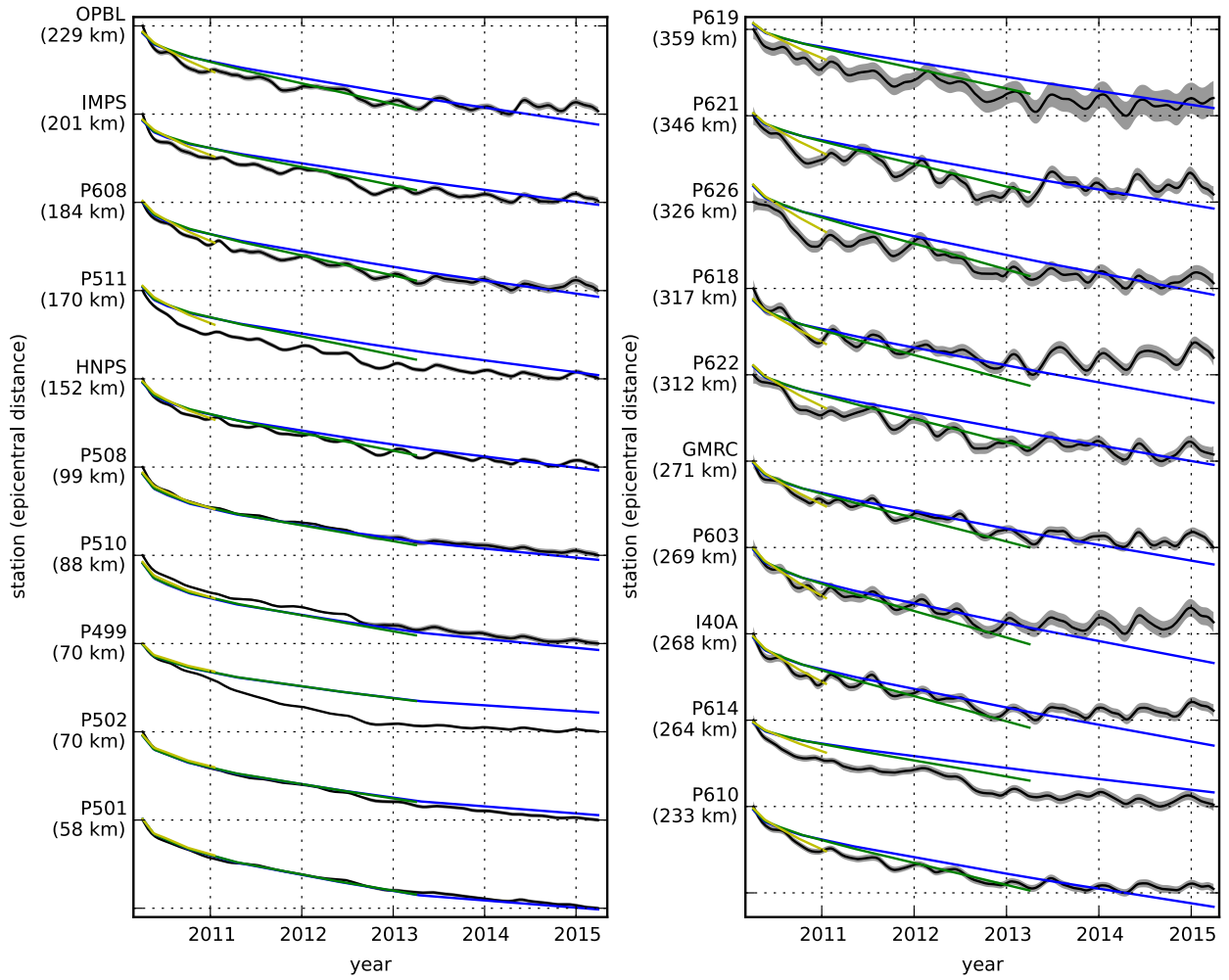
We estimate coseismic slip, afterslip, and effective viscosities by solving

$$\min_{s, \eta_{eff}} \left( \left\| \frac{u_{pred}(s, \eta_{eff}) - u_{post}}{\sigma_{post}} \right\|_2^2 + \lambda_s \|s\|_2^2 + \lambda_\eta \|\nabla \eta_{eff}^{-1}\|_2^2 \right), \quad (15)$$

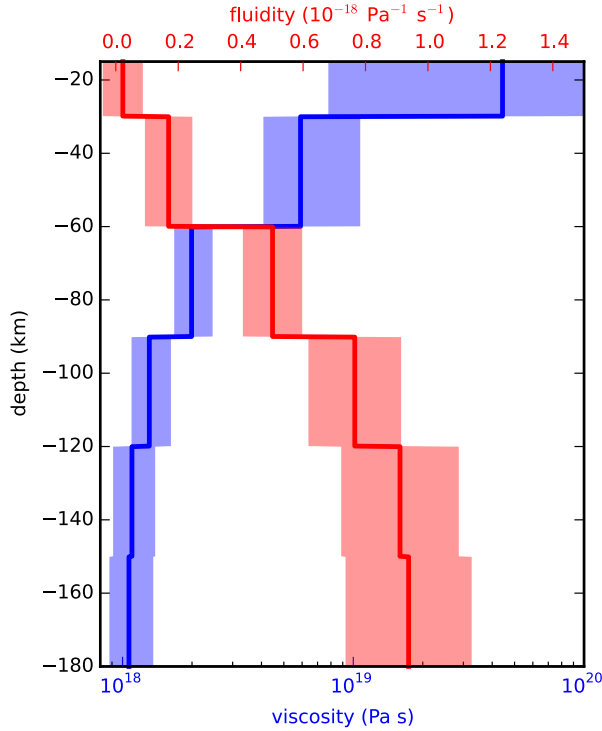
where  $u_{post}$  consists of the first 0.8 years of postseismic deformation and  $u_{pred}$  are the predicted displacements from eq. (14). Due to inherent non-uniqueness, we have added zeroth-order Tikhonov regularization to estimates of  $s$  and second-order Tikhonov regularization to estimates of effective fluidity  $\eta_{eff}^{-1}$ . The degree to which we impose the regularization on slip and fluidity is controlled by the penalty parameters  $\lambda_s$  and  $\lambda_\eta$ , which are chosen with trade-off curves. Our goal here is to get a prior constraint on  $\eta_{eff}$  to minimize the amount of searching we have to do when describing the postseismic deformation over the full five years, which we do in Section 3.3. Estimates of  $s$  made here will not be used in Section 3.3, and so the motivation behind adding regularization to  $s$  is to ensure that the slip driving viscoelastic relaxation in eq. (14) is sensible.

Our estimated effective viscosities, and corresponding fluidities, are shown in Figure 11. Although fluidity is rarely used in geophysical literature, eq. (13) is linear with respect to fluidity and so the fluidity indicates the amplitude of the viscoelastic signal coming from each layer. We also show the 95% confidence intervals for estimated viscosities and fluidities but we note that the uncertainties tend to be underestimated due to the added regularization [*Aster et al.*, 2011]. A robust feature that we see is that the largest jump in fluidity is at 60 km depth, which is consistent with the range of lithosphere-asthenosphere boundary depths inferred by *Lekic et al.* [2011]. This transitional depth is also consistent with the viscosity structure required to explain far-field postseismic deformation following the Hector Mine earthquake [*Freed et al.*, 2007]. We find that the viscosity below 60 km depth needs to be  $\sim 10^{18}$  Pa s to describe the early rate of postseismic deformation at far-field stations while the lower crust and uppermost mantle need to be relatively stronger. The viscosity of the lower crust is the least well constrained as there is no evidence of relaxation in that layer, meaning that it is effectively elastic over the first 0.8 years after the earthquake.

Our initial estimate for coseismic slip and cumulative afterslip over the first 0.8 years after the El Mayor-Cucapah earthquake are shown in Figure 12. Similar to our elastic slip model from Section 3.1, a significant amount of right-lateral and normal coseismic slip is inferred to be on the Sierra Cucapah fault segment. Our coseismic slip solution is consistent with field studies [*Fletcher et al.*, 2014] and the model from *Wei et al.* [2011b]. The potency of inferred



400 **Figure 10.** Observed postseismic displacements (black) and best fitting predictions of eq. (14) to 5.0 (blue),  
401 3.0 (green), and 0.8 (yellow) years of the postseismic data.



427      **Figure 11.** Effective viscosities and associated fluidities inferred by fitting eq. (14) to the first 0.8 years of  
428      postseismic displacements. 95% confidence intervals, estimated from bootstrapping, are indicated by color  
429      fields.

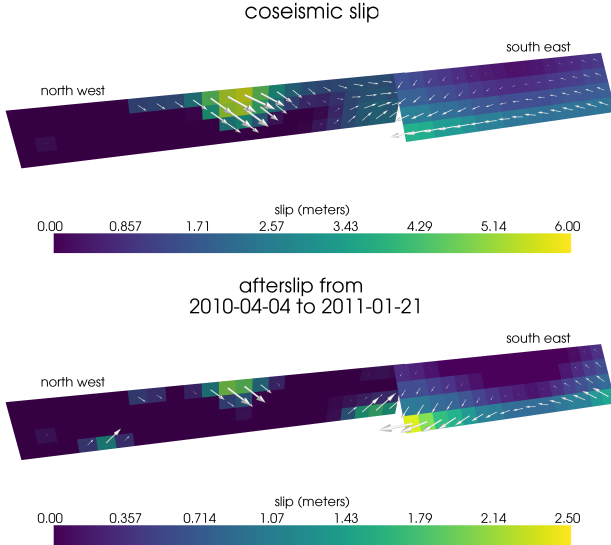
435      coseismic slip is  $3.3 \times 10^9 \text{ m}^3$ , which is also about the same as that inferred from Section  
436      3.1. The present inference of afterslip on the Indiviso fault is significantly less than what was  
437      found in the Section 3.1 where we did not account for viscoelasticity. When fault slip is si-  
438      multaneously estimated with viscosity, the potency of inferred afterslip over the first 0.8 years  
439      after the earthquake is  $0.85 \times 10^9 \text{ m}^3$ , compared to  $3.5 \times 10^9 \text{ m}^3$  when we assume the crust  
440      and upper mantle are elastic. The significant amount of afterslip inferred on the Indiviso fault  
441      seems to be compensating for unmodeled viscoelastic relaxation at depths greater than 60 km.  
442      The fact that there is still an appreciable amount of afterslip inferred on the Indiviso fault raises  
443      the question of whether it is compensating for viscoelastic relaxation that is more localized  
444      than what we allow for since we only estimate depth dependent variations in viscosity.

### 447      3.3 Full Postseismic Inversion

448      In the previous section, we used the inverse method from *Hines and Hetland* [2016] to  
449      constrain the effective viscosity structure required to explain the first 0.8 years of postseismic  
450      deformation. In this section, we use these effective viscosities as a prior constraint when search-  
451      ing for models which are capable of describing the available five years of postseismic data,  
452      where our forward problem is now eq. (11) rather than the approximation given by eq. (14).  
453      We perform a series of fault slip inversions assuming a variety of rheologies for the lower crust  
454      and upper mantle which are consistent with our findings from Section 3.2. We appraise each  
455      model using the mean chi-squared value,

$$\bar{\chi}^2 = \frac{1}{N} \left\| \frac{u_{\text{pred}} - u_{\text{obs}}}{\sigma_{\text{obs}}} \right\|_2^2, \quad (16)$$

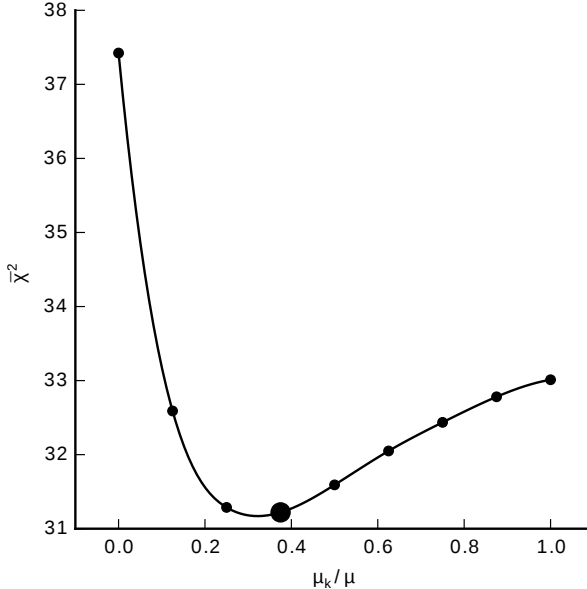
456      where  $N$  is the number of observations.



445 **Figure 12.** Coseismic slip and afterslip inferred by fitting eq. (14) to the first 0.8 years of postseismic  
446 displacements.

457 We first assume that the crust and mantle can be described with a Maxwell rheology,  
458 and we set the steady-state viscosity  $\eta_M$  equal to our inference of  $\eta_{\text{eff}}$ . We compute  $f$  and  $g$   
459 from eq. (11) using Pylith, and we use the same spatial and temporal discretization of  $s$  as  
460 in Sections 3.1 and 3.2. We estimate  $s$  using linear least squares and find a misfit of  $\bar{\chi}^2 =$   
461 37.4. For comparison,  $\bar{\chi}^2 = 35.3$  for the elastic model from Section 3.1. The Maxwell vis-  
462 coelastic model has a larger misfit because it tends to overestimate the rate of deformation af-  
463 ter about three years (Figure 7). Since our initial estimates of  $\eta_{\text{eff}}$  may be biased towards over-  
464 estimating viscosities, we have also performed the slip inversion where we use uniformly lower  
465 viscosities in the crust and mantle. However, decreasing the viscosity only increases the mis-  
466 fit. Although, the viscosities used here are consistent with the successful Maxwell viscoelas-  
467 tic models found by *Rollins et al.* [2015] and *Spinler et al.* [2015], which had mantle viscosi-  
468 ties on the order of  $10^{18}$  Pa s and relatively higher lower crustal viscosities, we find that such  
469 a model is incapable of describing the entire postseismic time series. *Pollitz et al.* [2001] sim-  
470 ilarly recognized this deficiency in a Maxwell rheology, which then motivated their exploration  
471 of a Burgers rheology upper mantle [Pollitz, 2003].

472 Instead of exploring a Burgers rheology mantle, which introduces two new parameters  
473 that need to be estimated, the transient viscosity  $\eta_K$  and transient shear modulus  $\mu_K$ , we first  
474 consider a Zener rheology for the mantle, which only introduces one additional unknown pa-  
475 rameter,  $\mu_K$ . We assume that the lower crust still has a Maxwell rheology. The steady-state  
476 viscosity in the crust and the transient viscosity in the mantle are set equal to the inferred ef-  
477 fective viscosities. We then estimate the ratio of shear moduli  $\frac{\mu_K}{\mu}$ . We compute nine differ-  
478 ent sets of Green's functions,  $f$  and  $g$ , where we assume values of  $\frac{\mu_K}{\mu}$  ranging from 0 to 1.  
479 The former being a degenerate case where the Zener model reduces to the above Maxwell model.  
480 We estimate coseismic slip and afterslip for each realization of  $\frac{\mu_K}{\mu}$ . The shear moduli ratio  
481 that yields the best prediction to the observed postseismic displacements is found to be 0.375  
482 which produces a misfit of  $\bar{\chi}^2 = 31.2$  (Figure 13). The improvement in the Zener model over  
483 the Maxwell model can be clearly seen in the fit to the far-field data (Figure 7). The Zener  
484 model does a significantly better job at explaining the transient rate of far-field deformation  
485 throughout the five years.

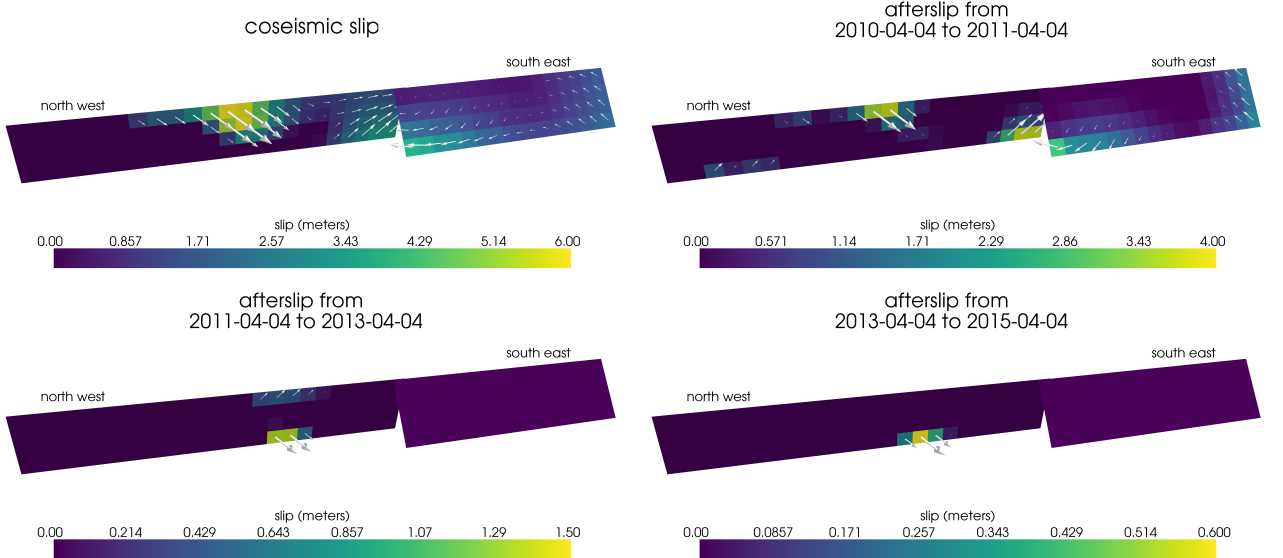


486 **Figure 13.** Mean chi-squared value for the best fitting slip model as a function of the transient shear modu-  
 487 lus relative to the elastic shear modulus in a Zener upper mantle. Large dot indicates our preferred ratio.

488 Because we are able to adequately describe the available five years of postseismic de-  
 489 formation with a Zener model, we do not find it necessary to explore the parameter space for  
 490 a more complicated Burgers rheology. However, since the Zener model is a Burgers model with  
 491 an infinite steady-state viscosity, we can conclude that any Burgers rheology that has a trans-  
 492 sient viscosity consistent with that found in Section 3.2 and a steady-state viscosity  $\gtrsim 10^{20}$   
 493 Pa s, which is effectively infinite on the time scale of five years, would also be able to sat-  
 494 isfactorily describe the observable postseismic deformation.

495 The regularized inference of coseismic slip and afterslip for our preferred Zener model  
 496 is shown in Figure 14. The inferred coseismic potency is  $3.0 \times 10^9$  m<sup>3</sup>, equivalent to a Mw=7.26  
 497 earthquake, and most of the slip is shallow and on the Sierra Cucapah fault segment. The po-  
 498 tency of five years of afterslip is  $1.1 \times 10^9$  m<sup>3</sup>. Most of the afterslip in our preferred model  
 499 occurs within the first year after the earthquake and coincides with the location of our inferred  
 500 coseismic slip. Inferred afterslip within the first year is accounting for the most rapid near-  
 501 field transient deformation. After one year, afterslip is inferred to be deeper down on the Sierra  
 502 Cucapah segment, which is describing much of the sustained near-field postseismic deforma-  
 503 tion. We emphasize, that the GPS station closest to where we infer afterslip, P496, is still about  
 504 30 km away, which is too far for us to conclusively argue for sustained localized deformation  
 505 rather than shallow distributed deformation. The deep afterslip inferred after one year could  
 506 potentially be describing deformation resulting from lower crustal flow. To test this, we have  
 507 modified our preferred model by decreasing the lower crustal viscosity from  $5.91 \times 10^{19}$  Pa  
 508 s to  $1 \times 10^{19}$  Pa s, which is still consistent with our viscosity inference from Section 3.2, and  
 509 inverted for fault slip. We find that a model with a weaker lower crust adequately describes  
 510 the postseismic displacements without any afterslip after one year, while still requiring about  
 511 the same amount of afterslip over the first year. We do believe that the early, shallow after-  
 512 slip on the Sierra Cucapah segment is a robust feature in our preferred model, while we are  
 513 not confident in our inference of later deep afterslip.

514 the postseismic displacements predicted by our preferred model are shown in Figures  
 515 4, 5 and 7. Overall, the trends in the near-field and far-field transient deformation are accu-  
 516 rately described. In particular, the trends in far-field deformation are much better described



530 **Figure 14.** Inferred coseismic slip and afterslip when assuming a Maxwell rheology in the lower crust and  
 531 a Zener rheology in the upper mantle. The transient viscosity  $\eta_K$  in the mantle and steady-state viscosity  $\eta_M$   
 532 in the crust are set equal to the effective viscosities from Figure 11. We set  $\frac{\mu_K}{\mu} = 0.375$  in the upper mantle.

517 by our preferred Zener model than either an elastic model or a model with a Maxwell viscoelastic-  
 518 mantle (Figure 7). There are a few areas where we have notable misfit. Most of our mis-  
 519 fit is for the near-field stations in the Imperial Valley, and we attribute this misfit to our rel-  
 520 atively simple fault geometry, which does not account for potential fault slip in the Imperial  
 521 Valley triggered by the El Mayor-Cucapah earthquake [Wei *et al.*, 2011a, 2015]. In particu-  
 522 lar, we are unable to model the sustained, rapid rate of deformation at station P496, which sug-  
 523 gests that this station could be influenced by a more localized deformation mechanism than  
 524 is considered in this study. Additionally, we see systematic misfit in the later postseismic pe-  
 525 riod west of the Landers and Hector Mine earthquakes, which may be the result of unmod-  
 526 eled postseismic deformation resulting from those earthquakes. Lastly, there are clear discrep-  
 527 ancies between the observed and predicted vertical deformation following the first year after  
 528 the El Mayor Cucapah earthquake. We observe a broad uplift throughout Southern Califor-  
 529 nia, which is inconsistent with any postseismic model.

#### 533 4 Discussion

534 It has long been recognized that deep afterslip and viscoelastic relaxation following an  
 535 upper crustal earthquake can result in similar horizontal ground deformation at the surface [e.g.  
 536 Savage, 1990; Pollitz *et al.*, 2001; Hearn, 2003; Feigl and Thatcher, 2006]. The similarity of  
 537 the horizontal postseismic deformation results in a non-uniqueness in inferences of afterslip  
 538 or viscoelastic relaxation. In contrast, the spatial pattern of vertical postseismic deformation  
 539 has been proposed to be a discriminant between deep afterslip and viscoelastic relaxation [e.g.  
 540 Pollitz *et al.*, 2001; Hearn, 2003]. It is, however, important to note that patterns of vertical de-  
 541 formation are very sensitive to the depth-dependence of viscosity below the upper crust [Yang  
 542 and Toksöz, 1981; Hetland and Zhang, 2014]. The similarity between deformation resulting  
 543 from deep afterslip and viscoelastic relaxation of coseismic stresses is different from the ill-  
 544 posedness described in Section 3.2. In our method, any inferred afterslip will also mechani-  
 545 cally drive additional viscoelastic relaxation. The horizontal deformation resulting from deep  
 546 afterslip will generally be in the opposite direction as horizontal deformation resulting from

547 viscoelastic relaxation of subsequent stresses in the lower crust (Figure 9). As a result, there  
 548 is a trade-off between inferences of deep afterslip and lower crustal viscosity. In our synthetic  
 549 tests in *Hines and Hetland* [2016], we have found that inverting surface deformation for af-  
 550 terslip and viscosity within the same depth interval tends to result in overestimated afterslip  
 551 and an underestimated viscosity.

552 Most postseismic studies assume Maxwell viscoelasticity in the lower crust and upper  
 553 mantle [e.g. *Nur and Mavko*, 1974; *Pollitz et al.*, 2000; *Hetland*, 2003; *Freed et al.*, 2006; *John-*  
 554 *son et al.*, 2009; *Hearn et al.*, 2009], which is the simplest viscoelastic rheologic model. In South-  
 555 ern California, postseismic studies following the Landers [*Pollitz et al.*, 2000], Hector Mine  
 556 [*Pollitz et al.*, 2001], and El Mayor-Cucapah earthquake [*Spinler et al.*, 2015; *Rollins et al.*, 2015],  
 557 have assumed Maxwell viscoelasticity in the lower crust and upper mantle and have inferred  
 558 upper mantle viscosities on the order of  $10^{17}$  to  $10^{18}$  Pa s and lower crust viscosities  $\gtrsim 10^{19}$   
 559 Pa s. These postseismic studies are consistent with *Kaufmann and Amelung* [2000] and *Cav-*  
 560 *alié et al.* [2007], who found that an upper mantle viscosity of  $10^{18}$  Pa s and a crustal viscos-  
 561 ity  $\gtrsim 10^{20}$  Pa s are necessary to describe subsidence resulting from changes in loading from  
 562 Lake Mead. This isostatic adjustment is a process with similar spatial and temporal scales as  
 563 postseismic deformation, and thus the inferred viscosities of these two types of studies would  
 564 likely agree. While these studies found viscosities that are consistent with our effective vis-  
 565 cosities from Section 3.2, they are inconsistent with viscosity estimates made from geophys-  
 566 ical processes that occur over longer time scales. For example, *Lundgren et al.* [2009] found  
 567 that lower crust and upper mantle viscosities on the order of  $10^{21}$  and  $10^{19}$  Pa s, respectively,  
 568 are needed to describe interseismic deformation along the Southern San Andreas fault zone  
 569 in the Salton Sea region. An even higher mantle viscosity, on the order of  $10^{20}$  Pa s, is re-  
 570 quired to describe isostatic adjustment resulting from the draining of Lake Bonneville, which  
 571 occurs on the time scales of  $10^4$  years [*Crittenden*, 1967; *Bills and May*, 1987].

572 An additional deficiency with the Maxwell rheology is that it predicts a steady decay  
 573 in the rate of postseismic deformation over time, which fails to describe the commonly ob-  
 574 served rapid, early transience followed by a relatively steady rate of postseismic deformation.  
 575 One could explain the early transient postseismic deformation with fault creep and the later  
 576 phase with relaxation in a Maxwell viscoelastic lower crust and upper mantle [e.g. *Hearn et al.*,  
 577 2009; *Johnson et al.*, 2009]. However, postseismic deformation at distances greater than  $\sim 200$   
 578 km from the El Mayor-Cucapah epicenter can only be attributed to viscoelastic relaxation [*Freed*  
 579 *et al.*, 2007] and we have demonstrated that the far-field deformation cannot be explained with  
 580 a Maxwell rheology (Figure 7).

581 We found that a Zener rheology in the upper mantle with a transient viscosity of  $\sim 10^{18}$   
 582 Pa s does a noticeably better job at predicting far-field postseismic deformation. A general-  
 583 ization of the Zener viscoelastic model, schematically represented as several Kelvin elements  
 584 connected in series, is commonly used to describe seismic attenuation [*Liu et al.*, 1976]. The  
 585 highest viscosity needed to describe seismic attenuation is on the order of  $10^{16}$  Pa s [*Yuen and*  
 586 *Peltier*, 1982] which has a characteristic relaxation time on the order of days. Even though  
 587 our inferred transient viscosity is orders of magnitude larger than that required for seismic at-  
 588 tenuation models, the two models are not incompatible. Rather, the delayed elasticity in seis-  
 589 mic attenuation models occurs on such short time scales that it can be considered part of the  
 590 instantaneous elastic phase of deformation associated with the preferred Zener model in this  
 591 study.

592 Of course, it has long been recognized that a Zener rheology provides an incomplete de-  
 593 scriptions of the asthenosphere, as it does not have the fluid-like behavior required to explain  
 594 isostatic rebound or convection in the mantle [*O'Connell*, 1971]. *Yuen and Peltier* [1982] pro-  
 595 posed a Burgers rheology with a low transient viscosity ( $\eta_K \approx 10^{16}$  Pa s) and high steady-  
 596 state viscosity ( $\eta_M \approx 10^{21}$  Pa s) to describe both seismic attenuation and long term geologic  
 597 processes. The justification of a Burger's rheology mantle is further supported by laboratory  
 598 experiments on olivine [*Chopra*, 1997]. *Pollitz* [2003] sought to describe postseismic defor-  
 599 mation following Hector Mine with a Burgers rheology mantle and they found a best fitting

transient viscosity of  $1.6 \times 10^{17}$  Pa s and steady-state viscosity of  $4.6 \times 10^{18}$  Pa s. While the Burgers rheology was introduced as a means of bridging the gap between relaxation observed in long and short term geophysical processes, the inferred steady state viscosity from Pollitz [2003] is still inconsistent with the Maxwell viscosities inferred from studies on the earthquake cycle and Lake Bonneville. The transient viscosity inferred by Pollitz [2003] is constrained by the earliest phase of postseismic deformation following the Hector Mine earthquake. While Pollitz [2003] ruled out deep afterslip as an alternative mechanism based on inconsistent vertical deformation, it is still possible to successfully describe all components of early postseismic deformation following the Hector Mine earthquake with afterslip at seismogenic depths [Jacobs *et al.*, 2002]. It is then possible that the preferred rheologic model from Pollitz [2003] was biased towards inferring a particularly low transient viscosity by neglecting to account for afterslip. This is in contrast to the present study, where we have inferred a viscosity structure simultaneously with afterslip. We also argue that a transient rheology is necessary to explain postseismic deformation; however, our preferred transient viscosity of  $\sim 10^{18}$  Pa s in the upper mantle is an order of magnitude larger than the transient viscosity found by Pollitz [2003]. Since a Zener model is able to describe the available postseismic deformation following the El Mayor-Cucapah earthquake, any Burgers rheology with a steady-state viscosity that is  $\gtrsim 10^{20}$  Pa s, effectively infinite over five years, would also be able to describe the postseismic deformation. Such a Burgers model might then be consistent with the steady-state viscosities necessary for lake loading, interseismic deformation, and mantle dynamics.

## 5 Conclusion

We have extracted a filtered and smoothed estimate of postseismic deformation following the El Mayor-Cucapah earthquake from GPS displacement time series. Our estimated postseismic deformation reveals far-field (epicentral distances beyond  $\sim 200$  km) transient deformation which is largely undetectable after about three years. Near-field deformation exhibits transience that decays to a sustained, elevated rate after about one or two years. We found that near-field transient deformation can be explained with shallow afterslip, and the sustained rate of near-field deformation can either be explained with continued afterslip or viscoelastic relaxation in the lower crust. Far-field transient deformation can be more definitively ascribed to viscoelastic relaxation at depths greater than  $\sim 60$  km. Beneath that depth, a transient viscosity of  $\sim 10^{18}$  Pa s is required to describe the rate of far-field deformation throughout the five years considered in this study. By describing the available postseismic deformation with a transient rheology in the mantle, our preferred model does not conflict with the generally higher steady-state viscosities inferred from geophysical processes occurring over longer time scales.

## Acknowledgements

We thank Andy Freed for an illuminating discussion on the data used in this study. This material is based on EarthScope Plate Boundary Observatory data services provided by UNAVCO through the GAGE Facility with support from the National Science Foundation (NSF) and National Aeronautics and Space Administration (NASA) under NSF Cooperative Agreement No. EAR-1261833. The data used in this study can be found at [www.unavco.org](http://www.unavco.org). This material is based upon work supported by the National Science Foundation under Grant Numbers EAR 1045372 and EAR 1245263.

## References

- Aagaard, B. T., M. G. Knepley, and C. A. Williams (2013). A domain decomposition approach to implementing fault slip in finite-element models of quasi-static and dynamic crustal deformation, *Journal of Geophysical Research: Solid Earth*, 118, doi: 10.1002/jgrb.50217.

- Argus, D. F., M. B. Heflin, G. Peltzer, F. Crampé, and F. H. Webb (2005), Interseismic strain accumulation and anthropogenic motion in metropolitan Los Angeles, *Journal of Geophysical Research: Solid Earth*, *110*(4), 1–26, doi:10.1029/2003JB002934.
- Aster, R. C., B. Borchers, and C. H. Thurber (2011), Parameter Estimation and Inverse Problems, vol. 90, Academic Press.
- Bawden, G. W., W. Thatcher, R. S. Stein, K. W. Hudnut, and G. Peltzer (2001), Tectonic contraction across Los Angeles after removal of groundwater pumping effects., *Nature*, *412*(August), 812–815, doi:10.1038/35090558.
- Bills, B. G., and G. M. May (1987), Lake Bonneville: Constraints on Lithospheric Thickness and Upper Mantle Viscosity From Isostatic Warping of Bonneville, Provo, and Gilbert Stage Shorelines, *Journal of Geophysical Research-Solid Earth and Planets*, *92*(B11), 11,493–11,508, doi:10.1029/JB092iB11p11493.
- Çakir, Z., S. Ergintav, H. Özener, U. Dogan, A. M. Akoglu, M. Meghraoui, and R. Reilinger (2012), Onset of aseismic creep on major strike-slip faults, *Geology*, *40*(12), 1115–1118, doi:10.1130/G33522.1.
- Cavalié, O., M. P. Doin, C. Lasserre, and P. Briole (2007), Ground motion measurement in the Lake Mead area, Nevada, by differential synthetic aperture radar interferometry time series analysis: Probing the lithosphere rheological structure, *Journal of Geophysical Research: Solid Earth*, *112*(3), 1–18, doi:10.1029/2006JB004344.
- Cetin, E., Z. Çakir, M. Meghraoui, S. Ergintav, and A. M. Akoglu (2014), Extent and distribution of aseismic slip on the İsmetpaşa segment of the North Anatolian Fault (Turkey) from Persistent Scatterer InSAR, *Geochemistry, Geophysics, Geosystems*, *15*, doi:10.1002/2014GC005307. Received.
- Chopra, P. N. (1997), High-temperature transient creep in olivine rocks, *Tectonophysics*, *279*, 93–111, doi:10.1016/S0040-1951(97)00134-0.
- Crittenden, M. (1967), Viscosity and Finite Strength of the Mantle as Determined from Water and Ice Loads\*, *Geophysical Journal of the Royal Astronomical ...*, pp. 261–279, doi:10.1111/j.1365-246X.1967.tb06243.x.
- Davis, J. L., B. P. Wernicke, and M. E. Tamisiea (2012), On seasonal signals in geodetic time series, *Journal of Geophysical Research: Solid Earth*, *117*(1), 1–10, doi:10.1029/2011JB008690.
- Feigl, K. L., and W. Thatcher (2006), Geodetic observations of post-seismic transients in the context of the earthquake deformation cycle, *Comptes Rendus - Geoscience*, *338*, 1012–1028, doi:10.1016/j.crte.2006.06.006.
- Fletcher, J. M., O. J. Teran, T. K. Rockwell, M. E. Osokin, K. W. Hudnut, K. J. Mueller, R. M. Spelz, S. O. Akciz, E. Masana, G. Faneros, E. J. Fielding, S. Leprince, A. E. Morelan, J. Stock, D. K. Lynch, A. J. Elliott, P. Gold, J. Liu-Zeng, A. González-Ortega, A. Hinojosa-Corona, and J. González-García (2014), Assembly of a large earthquake from a complex fault system: Surface rupture kinematics of the 4 April 2010 El Mayor-Cucapah (Mexico) Mw 7.2 earthquake, *Geosphere*, *10*(4), 797–827, doi:10.1130/GES00933.1.
- Freed, A. M., R. Bürgmann, E. Calais, J. Freymueller, and S. Hreinsdóttir (2006), Implications of deformation following the 2002 Denali, Alaska, earthquake for postseismic relaxation processes and lithospheric rheology, *Journal of Geophysical Research: Solid Earth*, *111*, 1–23, doi:10.1029/2005JB003894.
- Freed, A. M., R. Bürgmann, and T. Herring (2007), Far-reaching transient motions after Mojave earthquakes require broad mantle flow beneath a strong crust, *Geophysical Research Letters*, *34*, 1–5, doi:10.1029/2007GL030959.
- Gonzalez-Ortega, A., Y. Fialko, D. Sandwell, F. A. Nava-pichardo, J. Fletcher, J. Gonzalez-garcia, B. Lipovsky, M. Floyd, and G. Funning (2014), El Mayor-Cucapah (Mw7.2) earthquake: early near-field postseismic deformation from In-Sar and GPS observations, *Journal of Geophysical Research*, *119*, 1482–1497, doi:10.1002/2013JB010193. Received.

- 701 Hauksson, E., J. Stock, K. Hutton, W. Yang, J. A. Vidal-Villegas, and H. Kanamori  
 702 (2011), The 2010 Mw 7.2 El mayor-cucapah earthquake sequence, Baja California  
 703 Mexico and Southernmost California, USA: Active seismotectonics along the  
 704 Mexican pacific margin, *Pure and Applied Geophysics*, 168(3918), 1255–1277, doi:  
 705 10.1007/s00024-010-0209-7.
- 706 Hearn, E. H. (2003), What can GPS data tell us about the dynamics of post-seismic deforma-  
 707 tion ?, (2003), 753–777.
- 708 Hearn, E. H., S. McClusky, S. Ergintav, and R. E. Reilinger (2009), Izmit earthquake post-  
 709 seismic deformation and dynamics of the North Anatolian Fault Zone, *Journal of Geo-  
 710 physical Research: Solid Earth*, 114(August 2008), 1–21, doi:10.1029/2008JB006026.
- 711 Hetland, E. A. (2003), Postseismic relaxation across the Central Nevada Seismic Belt,  
 712 *Journal of Geophysical Research*, 108(Figure 2), 1–13, doi:10.1029/2002JB002257.
- 713 Hetland, E. A., and G. Zhang (2014), Effect of shear zones on post-seismic deformation  
 714 with application to the 1997 Mw 7.6 manyi earthquake, *Geophysical Journal Interna-  
 715 tional*, 198, 259–269, doi:10.1093/gji/ggu127.
- 716 Hines, T. T., and E. A. Hetland (2013), Bias in estimates of lithosphere viscosity from  
 717 interseismic deformation, *Geophysical Research Letters*, 40(16), 4260–4265, doi:  
 718 10.1002/grl.50839.
- 719 Hines, T. T., and E. A. Hetland (2016), Rapid and simultaneous estimation of fault slip  
 720 and heterogeneous lithospheric viscosity from post-seismic deformation, *Geophysical  
 721 Journal International*, 204(1), 569–582, doi:10.1093/gji/ggv477.
- 722 Jacobs, A., D. Sandwell, Y. Fialko, and L. Sichoux (2002), The 1999 (Mw7.1) Hector  
 723 Mine, California, Earthquake: Near-Field Postseismic Deformation from ERS Interfer-  
 724 ometry, *Bulletin of the Seismological Society of America*, 92(May), 1433–1442.
- 725 Johnson, K. M., and P. Segall (2004), Viscoelastic earthquake cycle models with deep  
 726 stress-driven creep along the San Andreas fault system, *Journal of Geophysical Research  
 727 B: Solid Earth*, 109, 1–19, doi:10.1029/2004JB003096.
- 728 Johnson, K. M., R. Bürgmann, and J. T. Freymueller (2009), Coupled afterslip and vis-  
 729 coelastic flow following the 2002 Denali Fault, Alaska earthquake, *Geophysical Journal  
 730 International*, 176(3), 670–682, doi:10.1111/j.1365-246X.2008.04029.x.
- 731 Jónsson, S., P. Segall, R. Pedersen, and G. Björnsson (2003), Post-earthquake ground  
 732 movements correlated to pore-pressure transients, *Nature*, 424(July), 179–183, doi:  
 733 10.1038/nature01758.1.
- 734 Kaufmann, G., and F. Amelung (2000), Reservoir-induced deformation and continental  
 735 rheology in vicinity of Lake Mead, Nevada, *Journal of Geophysical Research*, 105(B7),  
 736 16,341, doi:10.1029/2000JB900079.
- 737 Kroll, K. A., E. S. Cochran, K. B. Richards-Dinger, and D. F. Sumy (2013), Aftershocks  
 738 of the 2010 Mw 7.2 El Mayor-Cucapah earthquake reveal complex faulting in the Yuha  
 739 Desert, California, *Journal of Geophysical Research: Solid Earth*, 118(October), 6146–  
 740 6164, doi:10.1002/2013JB010529.
- 741 Lekic, V., S. W. French, and K. M. Fischer (2011), Lithospheric Thinning Beneath Rifted  
 742 Regions of Southern California, *Science*, 334(November), 783–787.
- 743 Liu, H.-P., D. L. Anderson, and H. Kanamori (1976), Velocity dispersion due to anelastic-  
 744 ity; implications for seismology and mantle composition, *Geophysical Journal Interna-  
 745 tional*, 47(1), 41–58, doi:10.1111/j.1365-246X.1976.tb01261.x.
- 746 Lundgren, P., E. A. Hetland, Z. Liu, and E. J. Fielding (2009), Southern San Andreas-San  
 747 Jacinto fault system slip rates estimated from earthquake cycle models constrained by  
 748 GPS and interferometric synthetic aperture radar observations, *Journal of Geophysical  
 749 Research: Solid Earth*, 114(2), 1–18, doi:10.1029/2008JB005996.
- 750 McGuire, J. J., and P. Segall (2003), Imaging of aseismic fault slip transients recorded  
 751 by dense geodetic networks, *Geophysical Journal International*, 155(3), 778–788, doi:  
 752 10.1111/j.1365-246X.2003.02022.x.
- 753 Meade, B. J., and B. H. Hager (2005), Block models of crustal motion in southern Cal-  
 754 ifornia constrained by GPS measurements, *Journal of Geophysical Research B: Solid*

- 755                          *Earth*, 110, 1–19, doi:10.1029/2004JB003209.
- 756 Murray, J. R., and P. Segall (2005), Spatiotemporal evolution of a transient slip event on  
757 the San Andreas fault near Parkfield, California, *Journal of Geophysical Research : Solid*  
758 *Earth*, 110(9), 1–12, doi:10.1029/2005JB003651.
- 759 Nur, A., and G. Mayko (1974), Postseismic viscoelastic rebound, *Science*, 183(4121),  
760 204–206, doi:10.1038/098448b0.
- 761 O'Connell, R. J. (1971), Rheology of the Mantle, *EOS, Transactions, American Geophysical Union*, 52, 140–142.
- 762 Osokin, M. E., J. R. Arrowsmith, A. Hinojosa Corona, A. J. Elliott, J. M. Fletcher, E. J.  
763 Fielding, P. O. Gold, J. J. Gonzalez Garcia, K. W. Hudnut, J. Liu-Zeng, and O. J. Teran  
764 (2012), Near-field deformation from the El Mayor-Cucapah earthquake revealed by  
765 differential LIDAR, *Science*, 335(6069), 702–705, doi:10.1126/science.1213778.
- 766 Pollitz, F., C. Wicks, and W. Thatcher (2001), Mantle Flow Beneath a Continental Strike-  
767 Slip Fault : Postseismic Deformation After the 1999 Hector Mine Earthquake, *Science*,  
768 1814(2001), 1814–1818, doi:10.1126/science.1061361.
- 769 Pollitz, F. F. (2003), Transient rheology of the uppermost mantle beneath the Mo-  
770 jave Desert, California, *Earth and Planetary Science Letters*, 215, 89–104, doi:  
771 10.1016/S0012-821X(03)00432-1.
- 772 Pollitz, F. F., G. Peltzer, and R. Bürgmann (2000), Mobility of continental mantle: Evi-  
773 dence from postseismic geodetic observations following the 1992 Landers earthquake,  
774 *Journal of Geophysical Research*, 105(1999), 8035, doi:10.1029/1999JB900380.
- 775 Pollitz, F. F., R. Bürgmann, and W. Thatcher (2012), Illumination of rheological mantle  
776 heterogeneity by the M7.2 2010 El Mayor-Cucapah earthquake, *Geochemistry, Geo-  
777 physics, Geosystems*, 13(6), 1–17, doi:10.1029/2012GC004139.
- 778 Rauch, H. E., F. Tung, and C. T. Striebel (1965), Maximum likelihood estimates of linear  
779 dynamic systems, *AIAA Journal*, 3(8), 1445–1450.
- 780 Riva, R. E. M., and R. Govers (2009), Relating viscosities from postseismic relaxation to  
781 a realistic viscosity structure for the lithosphere, *Geophysical Journal International*, 176,  
782 614–624, doi:10.1111/j.1365-246X.2008.04004.x.
- 783 Rollins, C., S. Barbot, and J.-P. Avouac (2015), Postseismic Deformation Following the  
784 2010 M7.2 El Mayor-Cucapah Earthquake : Observations , Kinematic Inversions , and  
785 Dynamic Models, *Pure and Applied Geophysics*, doi:10.1007/s00024-014-1005-6.
- 786 Savage, J. C. (1990), Equivalent strike-slip earthquake cycles in half-space and  
787 lithosphere-asthenosphere earth models, *Journal of Geophysical Research*, 95, 4873,  
788 doi:10.1029/JB095iB04p04873.
- 789 Savage, J. C., and J. L. Svart (2009), Postseismic relaxation following the 1992 M 7.3  
790 Landers and 1999 M 7.1 Hector Mine earthquakes , southern California, *Journal of*  
791 *Geophysical Research*, 114(B01401), doi:10.1029/2008JB005938.
- 792 Savage, J. C., J. L. Svart, and S. B. Yu (2005), Postseismic relaxation and transient creep,  
793 *Journal of Geophysical Research: Solid Earth*, 110, 1–14, doi:10.1029/2005JB003687.
- 794 Segall, P., and M. Mathews (1997), Time dependent inversion of geodetic data, *Journal of*  
795 *Geophysical Research*, 102.
- 796 Spinler, J. C., R. A. Bennett, C. Walls, L. Shawn, and J. J. G. Garcia (2015), As-  
797 sessing long-term postseismic deformation following the M7.2 4 April 2010, El  
798 Mayor-Cucapah earthquake with implications for lithospheric rheology in the  
799 Salton Trough, *Journal of Geophysical Research: Solid Earth*, 120, 3664–3679, doi:  
800 10.1002/2014JB011613.Received.
- 801 Wei, M., D. Sandwell, Y. Fialko, and R. Bilham (2011a), Slip on faults in the Imperial  
802 Valley triggered by the 4 April 2010 Mw 7.2 El Mayor-Cucapah earthquake revealed by  
803 InSAR, *Geophysical Research Letters*, 38(January), 1–6, doi:10.1029/2010GL045235.
- 804 Wei, M., Y. Liu, Y. Kaneko, J. J. McGuire, and R. Bilham (2015), Dynamic triggering of  
805 creep events in the Salton Trough, Southern California by regional M5.4 earthquakes  
806 constrained by geodetic observations and numerical simulations, *Earth and Planetary*  
807 *Science Letters*, 427, 1–10, doi:10.1016/j.epsl.2015.06.044.

- Wei, S., E. Fielding, S. Leprince, A. Sladen, J.-P. Avouac, D. Helmberger, E. Hauksson, R. Chu, M. Simons, K. Hudnut, T. Herring, and R. Briggs (2011b), Superficial simplicity of the 2010 El MayorCucapah earthquake of Baja California in Mexico, *Nature Geoscience*, 4(9), 615–618, doi:10.1038/ngeo1213.
- Yang M., and M. N. Toksöz (1981), Time-dependent deformation and stress relaxation after strike-slip earthquakes, *Journal of Geophysical Research*, 86, 2889–2901.
- Yuen, D. A., and W. R. Peltier (1982), Normal modes of the viscoelastic earth, *Geophysical Journal of the Royal Astronomical Society*, 69, 495–526, doi:10.1111/j.1365-246X.1982.tb04962.x.